Materials Horizons

ROYAL SOCIETY OF CHEMISTRY

REVIEW

View Article Online
View Journal | View Issue

Check for updates

Cite this: *Mater. Horiz.*, 2024, **11**, 1843

Received 30th September 2023,
Accepted 31st January 2024

DOI: 10.1039/d3mh01585h

rsc.li/materials-horizons

Evaporation-induced self-assembly of liquid crystal biopolymers

Soon Mo Park[ab] and Dong Ki Yoon *[a]

Evaporation-induced self-assembly (EISA) is a process that has gained significant attention in recent years due to its fundamental science and potential applications in materials science and nanotechnology. This technique involves controlled drying of a solution or dispersion of materials, forming structures with specific shapes and sizes. In particular, liquid crystal (LC) biopolymers have emerged as promising candidates for EISA due to their highly ordered structures and biocompatible properties after deposition. This review provides an overview of recent progress in the EISA of LC biopolymers, including DNA, nanocellulose, viruses, and other biopolymers. The underlying self-assembly mechanisms, the effects of different processing conditions, and the potential applications of the resulting structures are discussed.

Wider impact

Evaporation-induced self-assembly (EISA) has increasingly captured the spotlight owing to its foundational scientific principles and the vast potential it holds for application in materials science and nanotechnology. Notably, liquid crystal biopolymers have emerged as promising candidates for EISA, primarily due to their highly organized structures and the biocompatible nature they acquire post-deposition. The review at hand provides a comprehensive panorama of recent strides in EISA concerning liquid crystal biopolymers and the intrinsic mechanisms propelling self-assembly and explores the ramifications of diverse processing conditions. Looking ahead, the insights unveiled in this review are poised to play a pivotal role in steering the trajectory of materials science by informing strategic advancements and enabling tailored approaches within the burgeoning domain of evaporation-induced self-assembly.

1. Introduction

Evaporation of solutions is a natural phenomenon closely related to our life and fundamental science.[1,2] And it offers valuable insights for industrial applications, such as coating, printing, and patterning.[3–7] Thus, comprehending and effectively controlling the underlying principles of evaporation are essential. However, this proves to be challenging, given that diffusion and flow occur spontaneously during the drying and deposition processes.[8] Moreover, a solution's characteristics continuously change, including concentration, density, viscosity, and interfacial area.[9] To gain a comprehensive understanding of this spatiotemporal system, extensive research has been carried out on evaporation, delving into different aspects, encompassing initial concentrations,[10,11] solution components,[5,12] and boundary conditions.[13] Beyond internal factors, manipulating external conditions, such as temperature, humidity,[14] surface wettability,[10,15] and exposed interfacial area,[7] has led to intriguing phenomena. These phenomena include the Marangoni flows,[5,12,16] stick-and-slip motion,[10,11] and various deposition patterns.[6] Especially, in the deposition process, suspended particles exhibiting anisotropy develop condensed phases near the contact line, giving rise to unique morphologies that reflect the phase information.[17]

Anisotropic polymeric materials found in nature tend to undergo self-assembly once a specific concentration threshold is surpassed, displaying distinctive collective behavior owing to their unusual elasticity.[18,19] For instance, when a diluted deoxyribonucleic acid (DNA) aqueous solution is evaporated on a substrate, the DNA chains extend linearly along the moving direction of the contact line due to the receding force.[20,21] However, with an increase in the initial concentration, the DNA solution undergoes sequential transitions into chiral nematic and columnar phases during the drying process, and these structures in the phases are manifested in the resulting deposited film.[22] Moreover, biopolymers exhibiting cholesteric phases, such as cellulose nanocrystals and collagen, create diverse hierarchical structures not observed in the building blocks which can form only uniaxial alignment.[23–25] While their condensed phases, featuring various structural morphologies, have been

---

[a] *Department of Chemistry, Korea Advanced Institute of Science and Technology (KAIST), Daejeon, 34141, Republic of Korea. E-mail: nandk@kaist.ac.kr*
[b] *Department of Chemical and Biomolecular Engineering, Cornell University, Ithaca, NY, 14853, USA*

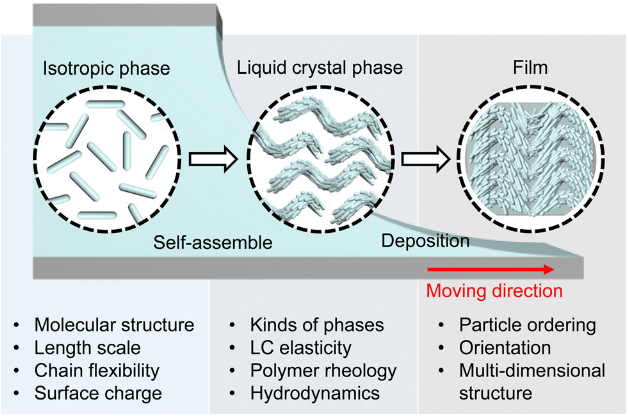

Fig. 1 Overview of evaporation-induced self-assembly of anisotropic biopolymers. The figure is reproduced from ref. 123 with permission from John Wiley and Sons, copyright 2021.

extensively studied in equilibrium systems, there are limited cases demonstrating collective behavior in dynamic systems, particularly regarding phase transition processes near the liquid–air interface. Hence, comprehensive insights can give protocols for the evaporation of various anisotropic biomaterials with inspiring related research.

Here, we present the evaporation-induced self-assembly (EISA) of representative biopolymers and colloids that reveal the liquid crystal (LC) phases (Fig. 1 and Table 1). First, we commence with an examination of the physical properties of aqueous biopolymer solutions such as hydrodynamics, rheology, and LC elasticity. This analysis explores molecular attributes such as the length scale, morphology, and surface chemistry, subsequently correlated with extensive research on lyotropic LC phases. We delineate anisotropic morphologies in the deposited film depending on the building blocks and highlight their potential for practical applications. Knowledge of evaporation holds significance not only for comprehending collective behavior within non-equilibrium systems but also for gaining fresh insights into leveraging biopolymers as fundamental building blocks in materials sciences.

2. Driving forces in EISA of anisotropic biopolymers

2.1. Hydrodynamics and rheological properties of the aqueous solution

We will introduce a comprehensive overview of EISA processes concerning anisotropic biopolymers and colloids, along with the resultant anisotropic structures observed in the deposited films. The flow of the liquid towards the contact line, driven by a surface tension gradient at the liquid–gas interfaces, causes the suspended solutes to condense.[8,9] It leads to a phase transition near the contact line, and the distinctive morphological patterns emerge as a manifestation of the liquid crystalline structures of the solutes during the drying process. To comprehend the underlying driving forces for these structures, our focus shifts toward investigating the self-assembly process within a non-equilibrium system. This inquiry is approached through the views of hydrodynamics, rheological analysis, and LC elasticity.

When positioning the initial concentration of the aqueous biopolymer solution in proximity to the nematic phase to initiate the self-assembly of LCs during the drying process, the solution exhibits a relatively high viscosity owing to the substantial macromolecular weight of the solute. This elevated viscosity correlates with a lower Reynolds number (Re), a parameter delineating flow conditions in hydrodynamics,[26]

$$\mathrm{Re} = \frac{\text{Inertia force}}{\text{viscous force}} = \frac{\rho v L}{\eta} < \mathcal{O}\left(10^{-6}\right)$$

where ρ is the mass density (kg m^{-3}, $\rho \sim \mathcal{O}\left(10^{3}\right)$), v is the flow velocity (m s^{-1}, $v \sim \mathcal{O}\left(10^{-6}\right)$), L is the length scale of the system (m, $L \sim \mathcal{O}\left(10^{-5}\right)$) and η is the solution dynamic viscosity (Pa s, $\eta \sim \mathcal{O}\left(10^{-1} \sim 10^{1}\right)$).

This elucidates that solute transportation during evaporation is primarily governed by capillary flow, transpiring along laminar capillary streamline pathways devoid of turbulence.

The capillary flow profile of (i) the sessile droplet, as well as (ii) under the meniscus curve in the coating process, can be assessed through height averaging when the solution undergoes evaporation under conditions of partial wetting (where the contact angle θ lies between 0° and 90°, Fig. 2a and b).

(i) Flow in a sessile droplet on a receding contact line. The evaporation of a sessile droplet on a substrate can be divided into two main steps: the pinned contact line step (constant contact line) and the moving contact line step (constant contact angle). We consider the average flow velocity of the droplet in the constant contact angle mode to compare with the solution coating velocity, where the meniscus curve moves continuously with the pulling speed. Below is one of the describing equations that have been reported (Fig. 2a),[27]

$$\bar{u}(r,t) = \frac{4D\Delta c}{\rho r \pi \theta}\left[\frac{1}{\sqrt{1 - r/R(t)^{2}}} + \frac{\frac{2}{3}(r/R(t))^{2} + \frac{1}{3}(r/R(t))^{4} - 1}{1 - (r/R(t))^{2}}\right]$$

where $\bar{u}$ is the height-averaged velocity of the internal fluid, D is the diffusion coefficient of vapor in the air (m^{2} s^{-1}), $\Delta c = c_{\mathrm{s}} - c_{\infty}$ is the difference of the saturated vapor concentration between just above the liquid–air interface and ambient air, θ is the contact angle, r is the distance from the center, and $R(t)$ is the radius depending on the time (m).

(ii) Flow in the meniscus-induced solution coating. Given that the volume of the loaded solution between two parallel substrates is adequate for accomplishing the coating process, the meniscus maintains a steady-state condition characterized by an unchanged shape over time. Consequently, the flow velocity beneath the meniscus curve could be evaluated by employing the Navier–Stokes equation with the lubrication approximation and the non-equilibrium one-sided (NEOS)

Table 1 Examples of evaporation-induced self-assembly of liquid crystal biopolymers

Category	Material specification	Methodology	Experimental condition	Driving force	Deposited structure	Ref.
DNA	λ-phage DNA (48.5 kbp, New England Biolabs Inc.)	Drop casting	Conc. 50 pg mL^{-1} Vol. 0.5 μL	Chain extension	Line pattern	155
	T4-phage DNA (166 kbp)	Drop casting	Conc. 0.1 μM Vol. 1 μL	Chain extension	Line pattern	156
	E. coli DNA	Sandwich cell (Thickness: 20 um)		Chain extension	Line pattern	20
	λ-phage DNA (48.5 kbp, New England Biolabs Inc.)	Template-assisted (Microchannel)	Δ Surface Hydrophilicity Δ Template geometry	Chain extension	Line-based various pattern	157
	λ-phage DNA (48.5 kbp, New England Biolabs Inc.)	Template-assisted (Micropost), Shear coating	Conc. 20-100 μg mL^{-1} Δ Template geometry	Chain extension	Line-based various pattern	158
	λ-phage DNA (48.5 kbp, GibcoBRL)	Spin coating	Conc. 0.4 μg mL^{-1}	Chain extenstion	Line pattern	159
	λ-phage DNA (48.5 kbp, New England Biolabs Inc.)	Blade coating	Conc. 5–10 μg mL^{-1}	Chain extension	Line pattern	160
	DNA sodium salt from salmon sperm (BioChem Co.)	Drop casting	Conc. 3.1–31 mg mL^{-1} Molecular weight 1.4–29 kbp	Nematic	Circular alignment	22
	λ-phage DNA (48.5 kbp, New England Biolabs Inc.)	Drop casting	Conc. 0.02–5 mg mL^{-1} Vol. 1–50 μL	Columnar	Zigzag alignment	42
	DNA (Chitose Institute of Science and Technology)	Shear coating	Conc. ∼20 wt %	Nematic	Uniaxial alignment	145
	DNA sodium salt from herring testes	Shear coating	Conc. 8 wt%	Nematic	Uniaxial alignment	161
	DNA sodium salt from calf thymus (Sigma Aldrich)	Shear coating	Conc. 200–300 mg mL^{-1}	Nematic	Uniaxial alignment	143
	DNA sodium salt from salmon testes (∼2000 bp, Sigma Aldrich)	Shear coating		Nematic and columnar	Uniaxial and zigzag alignment	71, 72 and 162
	DNA sodium salt from salmon testes (∼2000 bp, Sigma Aldrich)	Template-assisted (Microtemplate), Blade coating	Δ Template geometry	Nematic and columnar	Periodic two-dimensional structure	73 and 74
CNC	Cotton powder hydrolyzed by sulfuric acid	Drop casting, Sandwiched cell	Conc. 0.5–8 wt%	Nematic and Cholesteric	Circular alignment Radially aligned wavy structure (P ∼1–100 μm)	23
	Resinous tree hydrolyzed by sulfuric acid	Template-assisted (Petri dish)		Smectic and lamellar	Smectic-like and multilamellar structures	163
	Purified cellulose powder (CF-11; Whatman Co.) hydrolyzed by hydrobromic acid	Drop casting Shear coating	Additive (Polyvinyl alcohol, PVA)	Nematic	Circular and Uniaxial alignment	88
	Purified cellulose powder (CF-11; Whatman Co.) hydrolyzed by hydrobromic acid	Template-assisted (Embossed pattern)	Conc. 0.01–0.5 wt% of PVA	Nematic	Multi-directional alignment (parallel to the boundary condition)	89
	Wood pulp (CelluForce) hydrolyzed by sulfuric acid	Drop casting	Additives (PVA) Additives (Xylan) Conc. 0–10 mg mL^{-1} Temp. 20–60 °C Vol. 3–100 μL Δ Enzymatic reaction	Nematic	Uniaxial and multi-directional (orthogonal) alignment	90
	CNCs hydrolyzed by sulfuric acid (The University of Maine Process Development Center)	Drop casting	Conc. 0.1–3.9 wt% Vol. 0.25–5 μL Δ Substrate hydrophilicity	Nematic	Uniaxial and Multi-directional (orthogonal) alignment	87
	Microcrystal cellulose hydrolyzed by sulfuric acid (Sinopharm Chemical Reagent Co.)	Drop casting	Conc. 10 mg mL^{-1} Temp. 25–65 °C Vol. 10^{-4}–10^{2} μL	Nematic	Circular alignment	92
			Conc. 9 mg mL^{-1}	Nematic		93

Table 1 (*continued*)

Category	Material specification	Methodology	Experimental condition	Driving force	Deposited structure	Ref.
	Microcrystal cellulose hydrolyzed by sulfuric acid (Thermo Fisher Scientific)	Template-assisted (Spatial confinement)	Vol. 1–10 μL		Tailored circular and multi-directional alignment (parallel to the boundary condition)	
	Softwood sulfite pulp lapsheets hydrolyzed by sulfuric acid (Temalfa 93, Tembec Inc.)	Template-assisted (Petri dish)	Conc. 10 mL	Cholesteric	Parabolic focal conic structure	164
	Cellulose hydrolyzed by sulfuric acid (The U.S. Forest Products Laboratory at University of Maine)	Drop casting	Conc. 6 wt% Vol. 50 μL	Cholesteric	Polydomain structure with fingerprint texture	165
Amyloid fibrils	Protein extracted from β-Lactoglobulin	Drop casting	Conc. 2 wt% Vol. 5 μL	Cholesteric	Cholesteric fingerprint and Parabolic focal conic structure (P ~2–6 μm)	108
	Protein extracted from β-Lactoglobulin	Template-assisted (Sandwiched cell, Microchannel)	Δ Template geometry	Nematic	Uniaxial alignment Line-shaped structure (P ~10–100 μm)	109
Tobacco Mosaic Virus (TMV)		Drop casting	Vol. 20–30 uL Conc. 0.5–50 mg mL^{-1}	Nematic	Uniaxial, zigzag, and LC defect-like alignment	166
		Template-assisted (Capillary tube)		Nematic	Periodic band structure and multi-directional (Orthogonal) alignment	167
M13 Bacteriophage	Engineered M13KE phage (New England Biolabs Inc.) amplified by *E. Coli*	Template-assisted (Microtube)	Conc. 1–10 mg mL^{-1}	Chiral smectic C	Zigzag, helicoidal, and vertical-striped structures	119
	Engineered M13KE phage (New England Biolabs Inc.) amplified by E. Coli	Droplet		Smectic	Nematic and Smectic-like structure	168
	Engineered M13KE phage (New England Biolabs Inc.) amplified by *E. Coli*	Droplet Solution Coating process		Smectic	Nematic and Smectic-like structure	169
	Engineered M13KE phage (New England Biolabs Inc.) amplified by *E. Coli*	Solution (Dip) coating process	Conc. 0.1–6 mg mL^{-1} Coating speed 1–100 μm min^{-1}	Nematic	Nematic orthogonal twist Cholesteric helical ribbon Smectic helicoidal nanofilament (P ~100–200 μm)	120
	Engineered M13KE phage (New England Biolabs Inc.) amplified by *E. Coli*	Solution (Dip/blade) Coating process	Conc. 5-20 mg mL^{-1} Coating speed 3–18 μm s^{-1}	Cholesteric	Helicoidal structure (P~ 1–10 μm)	123
	Engineered M13KE phage (New England Biolabs Inc.) amplified by *E. Coli*	Solution (Dip) coating process	Conc. 0.1–1 mg mL^{-1} Coating speed 0.01–5 mm min^{-1} Ionic strength 0.001–10 mM	Nematic and cholesteric	Two-dimensional dot pattern Smectic-like and arch-shaped structures (P~ 50–200 μm)	122
Collagen fibrils	Type 1 from calf skin	Drop casting	Conc. 10 mg mL^{-1} Vol. 50 μL pH 3–7	Cholesteric	Undulating and arch-shaped structure (P ~1–10 μm)	130
	Type 1 from calf skin	Template-assisted (Sandwiched cell)	Conc. 5 mg mL^{-1} pH 3	Cholesteric	Undulating and helicoidal structure (P ~ 1–10 μm)	125
	90% Type 1 and 10% Type 2 from steer skin	Drop casting	Conc. 0.005–23 mg mL^{-1} Vol. 30–50 μL Δ Evaporation rate	Cholesteric	Concentric ring pattern Undulating structure (P ~5–50 μm)	135
	Type 1 from rat tail tendons	Template-assisted (Microchamber)		Cholesteric	Arch-shaped structure	24
	Type 1 from rat tail tendons	Inkjet printing	Conc. 3.6–20 mg mL^{-1} Coating speed 20–100 mm s^{-1} Flow rate 0.05–0.5 mL min^{-1}	Cholesteric	Undulating structure (P~3–5 μm)	136

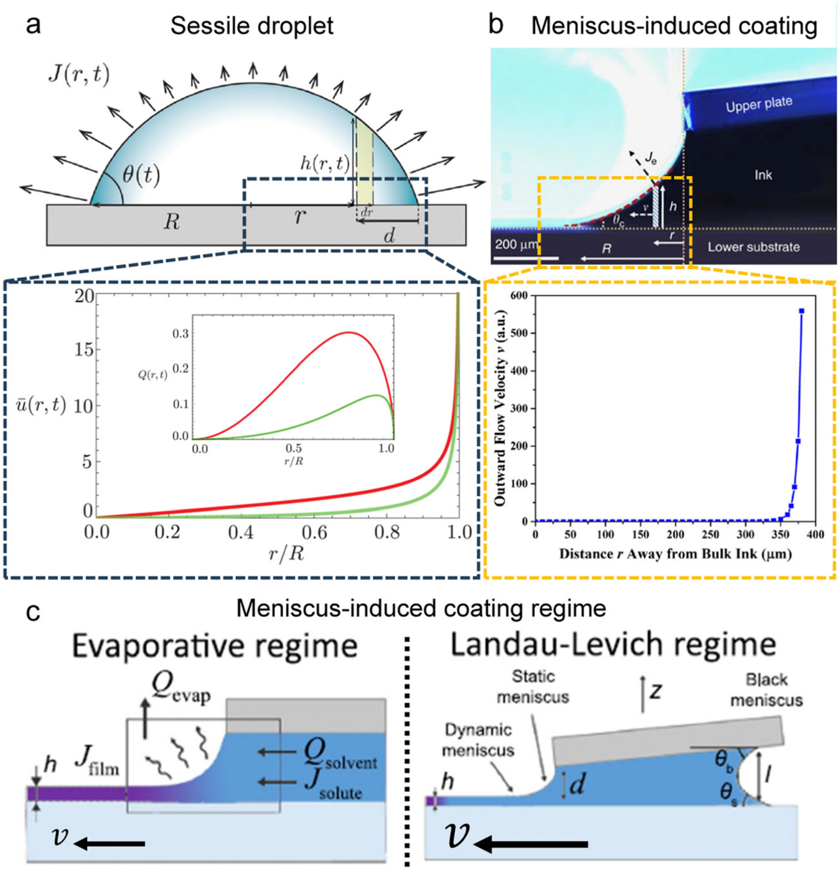

Fig. 2 Flow characterization in the drying process. Schematic illustration and internal velocity profile in the (a) partially wetted sessile droplet and (b) meniscus-assisted solution coating process. (c) Solution coating regime depending on the plate moving speed; evaporative regime and Landau–Levich regime. (a) Reproduced from ref. 28 with permission from The Royal Society of Chemistry, copyright 2022. (b) Reproduced from ref. 29 with permission from Springer Nature, copyright 2017. (c) Reproduced from ref. 33 with permission from Springer Nature, copyright 2018.

model (Fig. 2b),[28,29]

$$\bar{u}(r) = \frac{1}{\rho r h(r)} \int_0^r \left(\frac{r}{h(r)+K+W} \right) \mathrm{d}r$$

where $\bar{u}$ is the height-averaged velocity of the internal fluid and r is the distance from the edge of the blade. $h(r)$ is height under parabolic meniscus curve $h = a(R-r)^b$, where h is dependent on the moving speed of the lower substrate, K is the non-equilibrium parameter, W is the thermal effect given by $W = (kd_s)/(k_s d_0)$ (k is the liquid thermal conductivity, k_s is the thermal conductivity of the substrate, d_0 is the liquid thickness and d_s is the thickness of the substrate). For water, $K + W \sim \mathcal{O}(10^1)$.

Both estimations reveal a pronounced increase in fluid velocity in the evaporation process in proximity to the contact line.[27,29] This phenomenon underscores that the flow in the vicinity of the contact line, coupled with the concentration increase owing to evaporation, can trigger solute condensation and induce a phase transition into the LC phase. This concurs with the experimentally observed phase transition within the micrometre-scale ($(10^{-6}$–$10^{-4})$ m) distanced from the contact line. It implies that to control the alignment of the solutes in the deposited film, the self-assembly phenomena occurring in the region should be controlled.

During the coating process, the moving velocity of the substrate can be regulated, exerting an influence on the alignment of the solutes before deposition. When examining the capillary number (Ca) for the aqueous biopolymer solution within this system, which gauges the relative impact of viscous drag forces against surface tension forces operating at the liquid–gas interface,[16,27] it becomes evident that its value ranges from 10^{-4} to 10^{-2}. This range presents still in the capillary force-dominant region but can be close to the intermediate state, particularly if the velocity increases an order of magnitude in the micrometers per second range.[30] Consequently, the number means that manipulating the coating velocity empowers the control of the forces governing the self-assembly process through evaporation,

$$\mathrm{Ca} = \frac{\text{viscous drag force}}{\text{surface tension force}} = \frac{\eta v}{\sigma} \sim \mathcal{O}\left(10^{-4} \sim 10^{-2}\right)$$

where σ is the surface tension (N m^{-1}, $\sigma \sim \mathcal{O}(10^{-2})$ and v is the moving speed (m s^{-1}, $v \sim \mathcal{O}(10^{-5})$).

Indeed, within the coating process, two distinct regimes emerge depending on the moving velocity: the evaporation regime, characterized by the capillary assembly of solutes, and the Landau–Levich regime, signifying deposition through drag (Fig. 2c). The boundary defining their transition is termed the cross-over velocity, denoted as V_c,[31–33]

$$V_{\mathrm{c}} = \left[\left(\frac{\sigma^{2/3}}{\eta^{2/3}\kappa^{-1}}\right)\left(\frac{{J_0}^2}{\theta}\right)\right]^{\frac{3}{8}} \sim \mathcal{O}\left(10^{-6} \sim 10^{-5}\right)$$

where $\kappa^{-1} = \sqrt{\gamma/\rho g}$ is the capillary length (m, $\kappa^{-1} \sim \mathcal{O}\left(10^{-3}\right)$) and g is the gravitational acceleration. J_0 is given by $J_0 = Dc_\infty/\sqrt{\lambda}\rho$ related to the evaporation flux of water. For water, $J_0 \sim \mathcal{O}\left(10^{-9}\right)$. θ is the contact angle.

For aqueous biopolymer solutions, the estimated V_c is in the proximity of 10 μm s^{-1}, aligning with the boundary velocity experimentally observed to trigger a shift in the LC orientation in the deposited film. In the Landau–Levich regime ($v > V_c$), non-volatile solutes become kinetically quenched at the dragged meniscus before completely dehydrating. It leads to the orientation parallel to the coating direction. Conversely, in the evaporation regime ($v < V_c$), the solutes are afforded ample time for aggregation and self-assembly near the contact line. This temporal difference in behavior potentially clarifies the dependence on the flow dynamics of LC self-assembly of the solutes.

2.2. Liquid crystal elasticity of anisotropic biopolymers and colloids

In the drying process, the LC phases of the anisotropic biopolymers are developed near the contact line due to the flow-induced condensation, and the morphologies are directly reflected in the deposited film. The foundational LC and molecular anisotropy model is rooted in Onsager's approach, specifically targeting monodisperse infinite hard rods.[34] Following the theorem, researchers have advanced this framework by introducing an extension that accommodates the finite length scales and flexibility of solutes, which is gauged by contour length (ι), diameter (d), and persistence length (p).[35–39] Their study unveiled that this flexibility factor ($\alpha = l/p$) contributed to the increased critical concentration and a corresponding decrease in the order parameter based on the Onsager criteria,

$$\text{if } \alpha > 1, \quad \phi \times \frac{l}{d} \geq \text{constant}(\sim 4)$$

$$\text{if } \alpha \leq 1, \quad \phi \times \frac{p}{d} \geq \text{constant}(\sim 4)$$

where ϕ is the volume fraction of the solutes, d is the diameter (m), l is the contour length of the biopolymer (m), and p is the persistence length (m).

The LC building blocks align themselves parallel to the direction of the capillary flow streamline in order to minimize rotational resistance.[40,41] Meanwhile, the solutes present in the LC phases undergo splay deformation due to the convergence of meniscus towards the solid–liquid–air triple point on the substrate (Fig. 3a). The collective behavior exhibited by liquid crystalline biopolymers throughout the drying process can be described through the integration of the Frank–Oseen elastic energy (F) coupled with condensation effects.[42] Notably, the modified equation captures the phenomenon of solute condensation induced by capillary flow, which subsequently accelerates the elastic instability of the system beneath the meniscus curve,

$$F = \frac{K_1}{2}(\nabla \cdot \hat{n})^2 + \frac{K_2}{2}(\hat{n} \cdot (\nabla \times \hat{n}))^2 + \frac{K_3}{2}(\hat{n} \times (\nabla \times \hat{n}))^2 + \frac{E}{2}\frac{\partial\rho}{\rho^0}\lim_{x\to\infty}$$

where K_1, K_2 and K_3 are the elastic moduli for splay, twist and bend deformation, respectively, and $\partial\rho$ is the variation in the local solute density, ρ^0 is the mean solute density, and E is an elastic compressibility induced by external stress.

In this formula, the elastic constants of the liquid crystal are associated with factors such as the volume fraction and length scales.[43,44] Discrepancies persist between theoretical models and experimental measurements in the interpretation of 'semi-flexible' criteria ($\iota \sim \alpha^* p$), where α is the constant.[36,37] Nevertheless, we choose to simplify matters by directly comparing the contour length (l) to the persistence length (p) (Fig. 3b).

(i) The elastic constants of rigid LC polymers ($l < p$)

$$K_1 = \frac{7}{8\pi}\frac{k_{\mathrm{B}}T}{d}\phi\frac{l}{d}, K_2 = \frac{7}{24\pi}\frac{k_{\mathrm{B}}T}{d}\phi\frac{l}{d}, K_3 = \frac{7}{3\pi^2}\frac{k_{\mathrm{B}}T}{d}\phi^3\left(\frac{l}{d}\right)^3$$

(ii) The elastic constants of (semi-) flexible LC polymers ($l > p$)

$$K_1 = \frac{4}{\pi}\frac{k_{\mathrm{B}}T}{d}\phi\frac{l}{d}, \quad K_2 = \frac{k_{\mathrm{B}}T}{d}\phi^{\frac{1}{3}}\left(\frac{p}{d}\right)^{\frac{1}{3}}, \quad K_3 = \frac{4}{\pi}\frac{k_{\mathrm{B}}T}{d}\phi\frac{p}{d}$$

where k_{B} is the Boltzmann constant, and T is the temperature (K).

By directly comparing the relaxation time of splay deformations with the duration leading to the kinetically quenched state during the drying process, it would yield the most precise insight into the formation of an anisotropic structure within the deposited film.[45] Unfortunately, due to the current lack of analytical methods for such assessments, our approach is to focus on comprehending the system through the Ericksen number (Fig. 3c).[46,47] This dimensionless number effectively characterizes the interplay between LC elasticity and capillary-induced viscous forces that emerge during evaporation. The LC elasticity could be estimated through the elastic constants of the deformations, and although the numbers are around the unity, we could discern which force slightly dominates this system depending on the coating speed,

$$\mathrm{Er} = \frac{\text{Viscous force}}{\text{Elastic force}} = \frac{\eta v L}{K} \sim \mathcal{O}\left(10^{-1} \sim 10^{1}\right)$$

where K is the LC elasticity (N).

Our focus has been on discerning Ericksen numbers by employing carefully chosen papers, enabling us to estimate and correlate these values with the orientation of biopolymers within deposited films (Table 2). Examples in the table about the ambient drying of biopolymer solutions reveal Ericksen numbers spanning 0.1 to 10. The numerical values exhibit

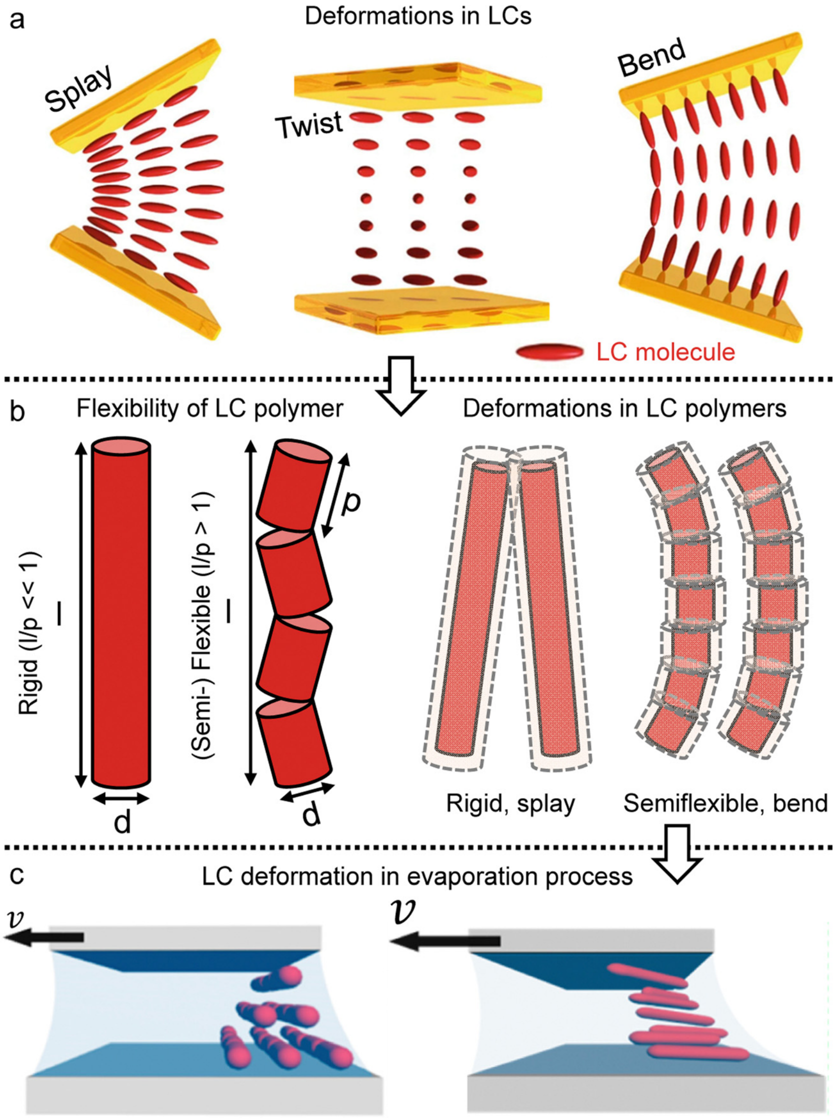

Fig. 3 LC polymer elasticity in the drying process. (a) Three kinds of director deformation in the liquid crystal phase; splay, twist, and bend. (b) Length scales of rod-like particles and examples of the LC polymer configuration under deformation. (c) Schematic illustration of LC directors depending on the solution coating speed. (a) Reproduced from ref. 41 with permission from Springer Nature, copyright 2019. (c) Reproduced from ref. 47 with permission from American Chemical Society, copyright 2017.

Table 2 Estimated Ericksen number of liquid crystal biopolymers in the solution coating process

Building block	Diameter (nm)	Contour length (nm)	Persistence length (nm)	Viscosity @ LC (Pa*s)	Dewetting velocity (μm s^{-1})	Film thickness (μm)	LC elasticity (pN)	Ericksen number, Er	Molecular alignment	Ref.
Salmon sperm DNA	2	680	50	$\mathcal{O}(10)$@50mg mL^{-1}	1–10	∼3	∼16.7	$Er_{\nu=1\,\mu m\,s^{-1}} \sim 1.8$ $Er_{\nu=10\,\mu m\,s^{-1}} \sim 1.8$	$n_{LC} \perp \vec{\nu}$ $n_{LC} \parallel \vec{\nu}$	72 and 145
Cellulose nanocrystals	10	100	2800	$\mathcal{O}(0.1)$@15mg mL^{-1}	5	∼10	∼0.5	$Er_{\nu=2\,\mu m\,s^{-1}} \sim 4$	$n_{LC} \perp \vec{\nu}$	91
Protein amyloids	3	300	1980	$\mathcal{O}(0.1)$@30mg mL^{-1}	∼1	∼1	∼0.5	$Er_{\nu=1\,\mu m\,s^{-1}} \sim 0.2$	$n_{LC} \perp \vec{\nu}$	109
M13 bacteriophage	6.6	880	2200	$\mathcal{O}(1)$@15mg mL^{-1}	3–18	∼3	∼15	$Er_{\nu=3\,\mu m\,s^{-1}} \sim 0.6$ $Er_{\nu=9\,\mu m\,s^{-1}} \sim 1.8$ $Er_{\nu=18\,\mu m\,s^{-1}} \sim 3.6$	$n_{LC} \perp \vec{\nu}$ n_{LC}: undulated $n_{LC} \parallel \vec{\nu}$	74
Collagen fibril	1.5	300	50–80	$\mathcal{O}(10)$@80mg mL^{-1}	∼2	∼1	∼0.5	$Er_{\nu=2\,\mu m\,s^{-1}} \sim 10$	n_{LC}: undulated	135

higher magnitudes when the orientation of building blocks aligns parallel to the coating direction. Conversely, in instances where the material orients perpendicular to the coating direction, the numbers generally range from 0.2 to 4. Additionally, an undulated structure in the cases of bacteriophage and collagen emerges under transient conditions between parallel and perpendicular alignments.

Our investigation affirms that the orientation of the biopolymers within the deposited film can be manipulated by the dominance of capillary flow and LC elasticity, irrespective of the atomic composition or molecular structure of the building blocks. Throughout the evaporation process, the orientation of the blocks aligns parallel to the capillary flow when viscous force dominates, whereas the dominance of elastic force results in alignment perpendicular to the flow direction (parallel to the contact line). Notably, the alignment is absent in cases of diluted concentration because it could be driven by the characteristics of collective behavior exhibited in the LC phases. Furthermore, in instances where the biopolymers form a helical structure, an undulated pattern reflective of the helicity manifests in a range in which viscous force and elasticity are balanced. Our findings elucidate the role of capillary flow and LC elasticity in governing chain orientation during the evaporation process and highlight the impact of chirality on the resultant film structure. In addition, the transient Ericksen number at cross-over velocities during the coating process suggests that theoretical estimations hold promise for interpreting biopolymer alignment in thin films.

3. Liquid crystal phases and anisotropic structure formation in EISA

3.1. Deoxyribonucleic acid (DNA)

Organisms have evolved various strategies to compress their genetic material, DNA, to the smallest possible cellular level: LC ordering,[48–53] supercoiling by entanglement,[54,55] hierarchical structure by DNA-histone interactions,[56,57] *etc.* Indeed, LC forms, one of the strategies for molecular compaction, have been found in sperm heads, chromosomes, and viruses (Fig. 4), where the compression efficiency of LC has allowed tens of thousands of base pairs with an overall contour length of a few microns to be packed into the capsids or heads of 50–100 nm. This ingenious packing not only efficiently stores genetic information but also protects the DNA from potential harm, including irradiation, oxidative agents, and degrading enzymes, because it reduces the accessibility of DNA molecules through structural sequestration.[58] In particular, the DNA LC expression has not only served important functions in living organisms, but has also helped to analyze the structure of DNA. When measuring X-ray diffraction patterns to analyze the structure of DNA chains, the chains could be aligned without interchain entanglement, which allowed for the formation of clear X-ray diffraction patterns.[59,60]

To understand the spontaneous phase transition to the ordered LC phases, numerous studies have revealed several distinct characteristics of these LCs *in vitro* (Fig. 5).[61–63] The emergence of the phases can be theoretically explained by

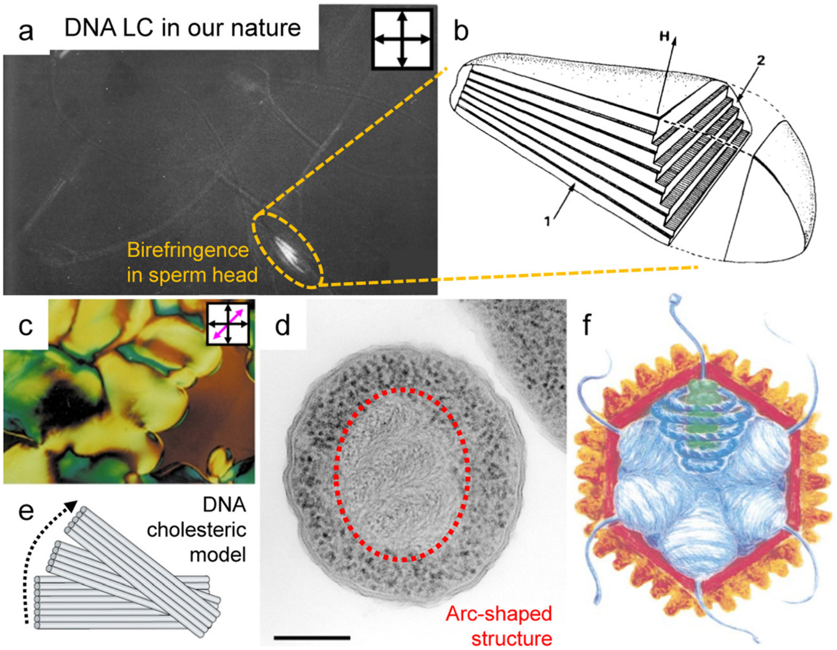

Fig. 4 DNA liquid crystal ordering in nature. (a) A polarized optical microscopy image (POM) of stallion spermatozoa. (b) Schematic illustration of DNA ordered structure in the sperm head. (c) The POM image of DNA liquid crystals purified from bacterial plasmids. (d) Arc-shaped DNA structure in starved Dps$^-$ *Escherichia coli* cell. (e) Partial alignment of DNA within consecutive layers that undergo continuous rotation in relation to each other. (f) Illustration for the DNA alignment in virus capsid. The blue coils present DNA indicating the 5-fold vertices within the core. (a) and (b) Reproduced from ref. 53 with permission from Elsevier, copyright 1984. (c)–(e) Reproduced from ref. 58 with permission from Springer Nature, copyright 2002. (f) Reproduced from ref. 52 with permission from Elsevier, copyright 1999.

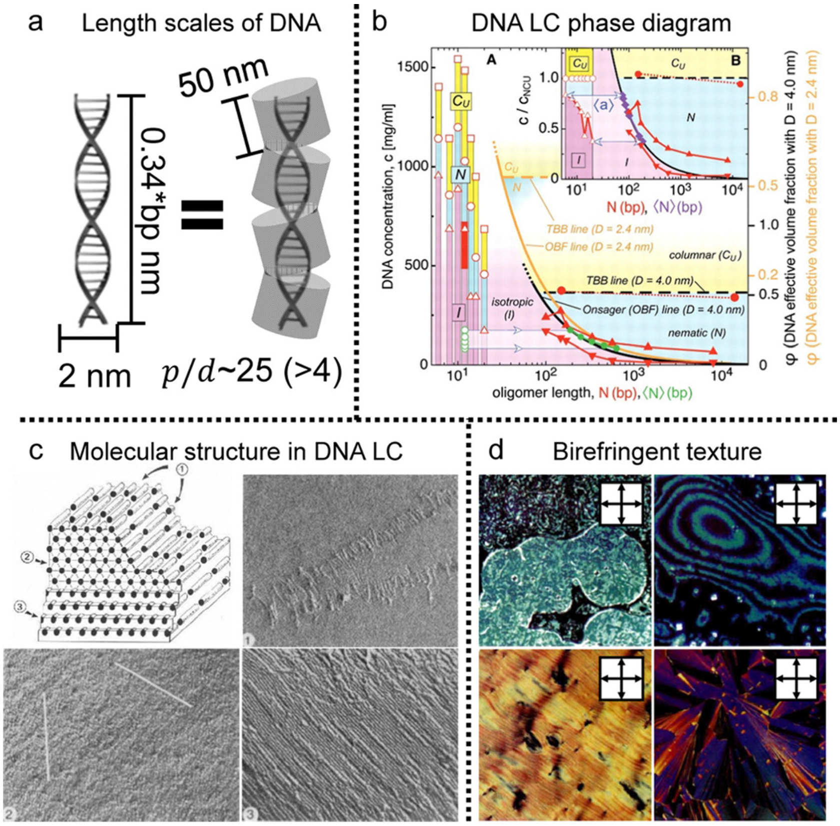

Fig. 5 DNA LC phases in vitro. (a) Length scale of DNA molecules. (bp: the number of base pairs) (b) liquid crystal phase diagram of DNA solution depending on concentration and contour length. (c) Schematic illustration of the highly concentrated liquid crystalline DNA structure. The number represent series of layers in the lamellar structure of the hexagonal phase. (d) Multiple morphologies of DNA liquid crystals observed under crossed polarizers. (b) Reproduced from ref. 65 with permission from Science, copyright 2006. (c) Reproduced from ref. 61 with permission from Springer Nature, copyright 1989. (d) Reproduced from ref. 63 with permission from Springer Nature, copyright 1988.

modelling the chain as the repulsive rigid or semi-flexible rod-like particle. The length scales of DNA chains with diameter ($d \sim 2$ nm), contour length ($l \sim 0.34$ * the number of base pairs (bp)), and persistence length ($p \sim 50$ m)[64] satisfied the condition for LC ordering as stated by the Onsager criteria (Fig. 5a). The critical volume fraction ($\varphi_{\mathrm{I-N}}$) marking the transition from the isotropic to nematic phase was found to be influenced by the number of base pairs below the persistence length.[65] In practical terms, this implies that exceeding 147 bp in a single DNA chain does not significantly vary the volume fraction compared to cases below 147. Depending on the concentration, different phases were identified, including nematic, cholesteric, and columnar, through polarizing optical and electron microscopy to obtain structural information based on the molecular structure (Fig. 5b–d).[61–63,65] Moreover, given the polyelectrolyte nature of DNA, its distinct traits were influenced by surrounding ionic contents that change the persistence length and the effective diameter of the DNA molecule.[66,67] Significant insights have emerged by investigating the rigid DNA fragments within differing ionic environments, such as interparticle spacing and phase boundary transition in the LC phases.[65,68] This behavior becomes more evident in various additives such as polyvalent cations (including polyamines), polymers, and organic solvents.[69] Those investigations also help to estimate the collective behavior of DNA in cholesteric and hexagonal columnar phases and semiflexible DNA chains with long contour lengths ($L/P > 1$). The flexibility does not fundamentally change the intrinsic properties of the LC phases (including the nematic and columnar hexagonal arrays), but it does affect the defect composition and rheological properties of the solution.

Based on the collective behavior of DNA LC in stable (metastable) states, people have tried to understand the interplay between their self-assembling behavior and evaporation-induced condensation. As mentioned in the introduction, the DNA chains were just stretched by the receding force of the contact line and deposited on the substrate in the drying process of the diluted DNA solution (Fig. 6a and b).[20,21,70] However, the evaporation of the concentrated solution is quite different from the diluted case because the initial concentration is high enough to induce the LC phase transition, in which the chains show collective behavior before thoroughly dehydrating.

Indeed, Morii *et al.* discovered, for the first time to my knowledge, the annular alignment of salmon sperm DNA chains in a drop-casting process (Fig. 6c).[22] They analyzed the DNA alignment in the deposited film as a function of the distance from the center of the circular film. They found

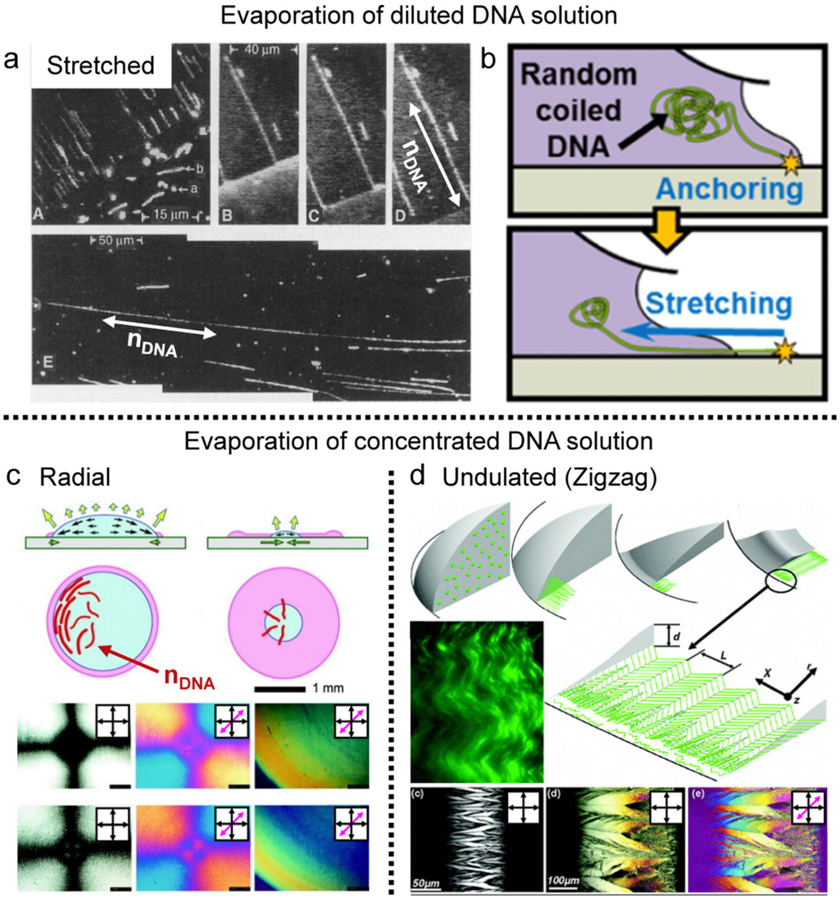

Fig. 6 Concentration-dependent DNA alignment in the deposited film. (a) The DNA chains deposited by drop-casting of diluted DNA solution. n_{DNA} represents the long axis of DNA molecules and the fluorescent dye-stained DNA chains are stretched along the contact line moving direction. (b) Schematic illustration of DNA chain extension in the drying process. (c) and (d) Self-assembly process and anisotropic structures of DNA chains in the deposited film. Red and light green lines in the illustration present the DNA molecules. (a) Reproduced from ref. 20 with permission from Science, copyright 1994. (b) Reproduced from ref. 70 with permission from American Chemical Society, copyright 2015. (c) Reproduced from ref. 22 with permission from John Wiley and Sons, copyright 2005. (d) Reproduced from ref. 42 with permission from American Physical Society, copyright 2006.

different structures depending on the initial concentration and temperature, one of which is orthogonal, with most molecular alignments being concentric but a small region near the center of the droplet being radially aligned. Based on the real-time observation, they proposed a possible mechanism for the chain orientation driven by a transitive balance of physical effects between the hydrodynamic forces and the Brownian motion of the chain segments. They found that an appropriate concentration to ensure mass diffusion and phase transition is essential and that highly dilute DNA solutions are unsuitable for forming oriented membranes.

Aligning to the above, Smalyukh *et al.* found a periodic zigzag structure in a ring-shaped deposit from DNA dry droplets (Fig. 6d).[42] In this study, Lambda-DNA, with 48 502 bp, shows a lyotropic liquid crystal around the contact line and aligns parallel to the boundary to minimize elastic energy. However, upon depinning, the radial dilative stress induces undulations at the rim, propagating inward through the columnar liquid crystal. They describe the structure formation through a model based on Frank–Oseen elastic energy with experimental results. The chain flexibility ($l/p > 300$) higher than the precedents might affect the formation of the micron-scale structure under the contact line receding force, not aligned parallel to the contact line.

Inspired by the pioneering works above, we have developed to fabricate periodic DNA microstructures in a long-range order (Fig. 7).[71–74] The brushing method allows reproducing the phenomenon by grooving the solution interface, which induces competitive interaction between compressive stress and DNA liquid crystal elasticity (Fig. 7a).[71] The line defects were induced by buckling instability of the columnar liquid crystal, and systematically studied the dimensional tunability along the width and depth of the micro-sized template. A solution coating process has been introduced to induce from uniaxial alignment to orthogonal orientation by controlling the moving velocity of the coating plate.[72] The combination with topographic templates could give a spatial confinement effect to the liquid crystal and deform the interfacial curvature of the solution (Fig. 7b and c).[73,74] The structural anisotropy can then be transferred, internally and externally, *e.g.*, to an alignment

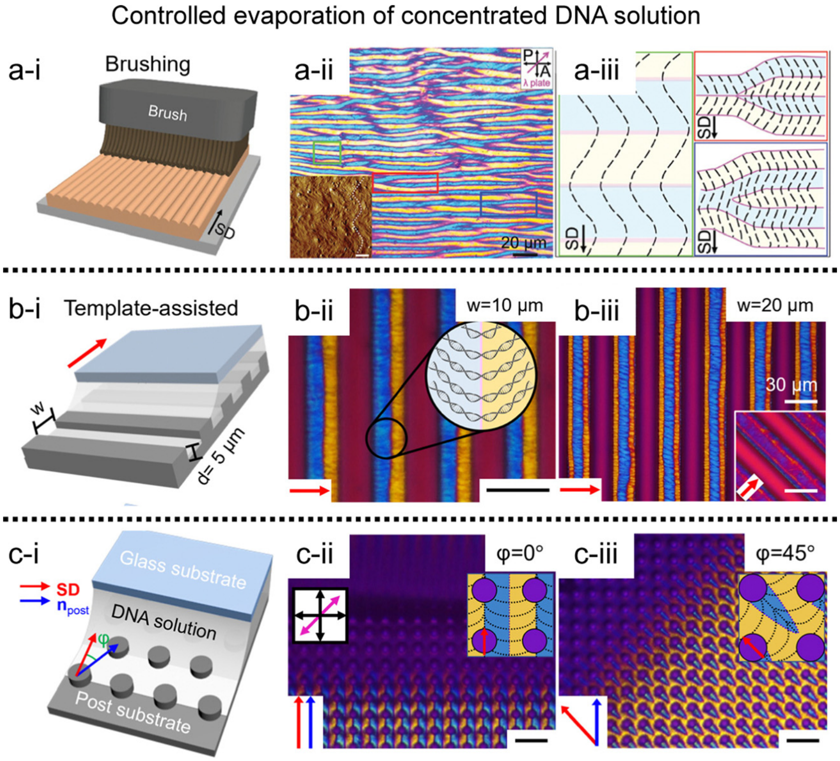

Fig. 7 Two-dimensional DNA LC structure. (a) Undulated zig-zag pattern in the brushed DNA film. (i) Schematic illustrations of the fabrication process, and (ii) and (iii) POM images and descriptions for DNA alignment. (b) and (c) Micro-sized periodic DNA structure on topographic templates; (b) microchannels, and (c) microposts. Black and red arrows represent the shear direction (SD), and black scale bars are 20 μm. (a) Reproduced from ref. 71 with permission from John Wiley and Sons, copyright 2017. (b) Reproduced from ref. 74 with permission from John Wiley and Sons, copyright 2020. (c) Reproduced from ref. 73 with permission from Springer Nature, copyright 2019.

layer, facilitating the alignment of nanomaterials on a surface or to a directional matrix, enabling their orientation within a mixture.

3.2. Nanocellulose

Cellulose, the most abundant biopolymer on our planet, is present in plants, marine environments, and products of bacteria.[75,76] The fibres of cellulose can be broken into controllable nanoscale building blocks called cellulose nanocrystals (CNCs) (Fig. 8a). These cellulose components, originating from renewable materials, possess not only eco-friendly benefits but also distinctive practical interest due to their various functional properties such as mechanical strength, optical and thermal properties.[77–80]

It is well-known that CNCs have the ability to self-assemble into a helical structure, which is referred to as chiral nematic or cholesteric phases (Fig. 8b) based on the twisting morphology of a single nanocrystal (Fig. 8c and d).[75,76,81,82] Such a hierarchical structure in the CNC matrix contributes to an iridescent color based on the periodicity of the refractive index (Bragg reflection), and researchers have tried to tune the pitch and tactoid formation to enhance their chiral optical activities.[83–86] Although much progress has been made with much effort, in this section, we will only discuss the unwind nematic order of CNCs induced by hydrodynamic flow and refer interested readers to the above available literature describing these cholesteric systems.

When drying sessile CNC dispersion droplets on the flat substrate, in-plane multiaxial alignment was found in the deposited film where the local director of CNCs is uniaxially aligned (Fig. 9a).[87] Pritchard *et al.* monitored the drying process in real-time through polarized optical microscopy (POM) and analyzed the drying dynamics using computational fluid dynamics. They utilized the Peclet number, a parameter comparing solute Brownian motion to capillary flow, to validate the dominant factor behind the sequential alignment of CNCs. They found that contact line behavior dominates the orthogonal alignment of CNCs in the deposition and studied various morphologies changing the initial concentration, surface wettability, and droplet volume. Also, there is another suggestion for the CNC alignment based on surface tension gradient-induced torque near the substrate–liquid–air interfaces.[88] The torque due to the surface tension getting higher close to the contact line rotates the CNCs perpendicular to the direction of the receding lines and parallels them to the solution boundary layer that matches with the behavior of splay relaxation.

To induce uniform alignment in the circular deposited film, researchers controlled the experimental systems *via* (i) the introduction of additives ref. 88–91 and (ii) surface modification using chemical treatment (acid hydrolysis) (Fig. 9b and c).[92,93]

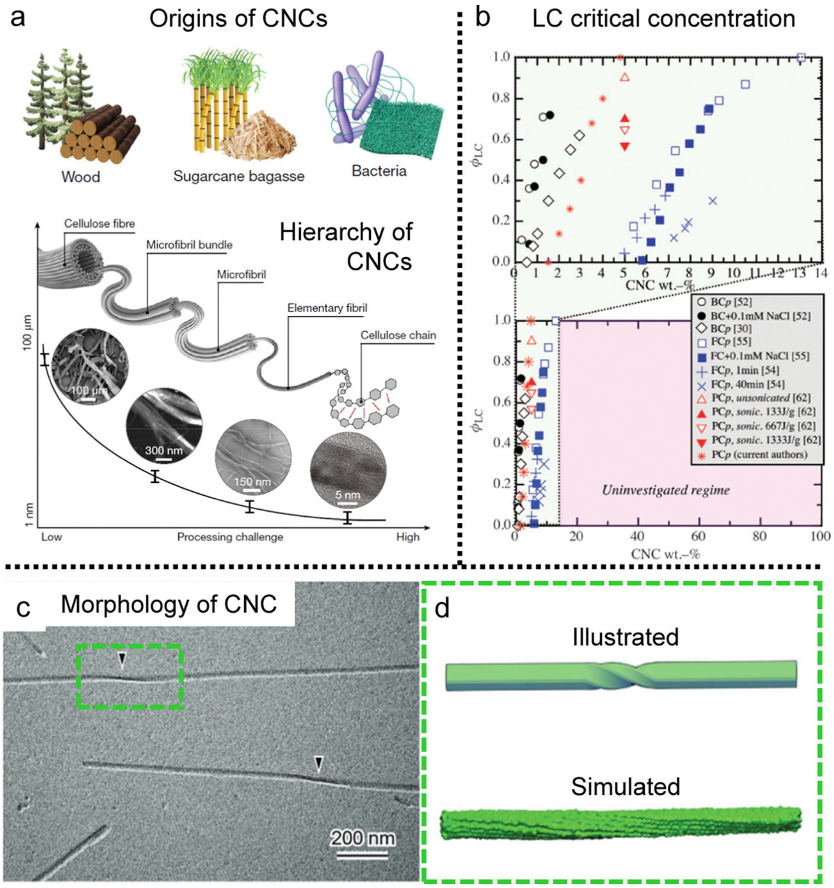

Fig. 8 Cellulose nanocrystal (CNC) building blocks. (a) The examples of origins of CNCs and the various length scales of CNCs depending on the fabrication process. (b) Liquid crystal phase transition diagram of CNCs depending on the origins and concentrations (BC: bacterial cellulose, FC: filter paper-derived cellulose, PC: wood pulp-derived cellulose, and the suffix p: pure without any additives). (c) CryoEM image of single CNCs. The black arrowheads point the twisted region. (d) Schematic illustration of the twisted morphology of single CNCs and simulated one showing right handedness based on molecular dynamics. (a) Is reproduced from ref. 76 with permission from Springer Nature, copyright 2021. (b) Reproduced from ref. 75 with permission from Springer Nature, copyright 2014. (c) and (d) Reproduced from ref. 78 with permission from Royal Society of Chemistry, copyright 2019.

(i) Introduction of additives. The water-soluble additives increase solution viscosity when mixing with the CNCs. The increased viscosity helps CNCs to align uniformly in the deposition process. After the dissolution of poly(vinyl alcohol) (PVA), individually dispersed PVA chains make a composite with CNCs tangentially aligned with uniformity.[89,90] The degree of alignment increases when PVA is mixed in the solution to increase the flexibility of the free-standing film. CNC alignment varies depending on a mixture of xylan, a hemicellulose family, with an enzyme. Talanikite *et al.* assayed a series of POM images of drop-cased films as a function of xylan concentration and found that at a certain ratio of the mixture, the Maltese cross pattern appeared different from a ring pattern of the pure CNC solution.[91] Although the alignment differs from the centre to edge, which is orthogonal in the film, the film thickness became flattened compared to the pure CNC solution. The introduction of xylan helps to increase the viscosity of the CNC solution, resulting in gel formation in the drying process. When they added xylanase, an enzyme of the water-soluble polymer, the enzymatic reaction successfully handled the self-assembly in the drying process, and the pattern and alignment returned to the original one due to the decreased molecular weight of xylan.

(ii) Surface modification using chemical modification. Surface-modified CNCs (M-CNCs) in which the sulfuric acid was replaced by carboxylic acid formed fully concentric alignment in a drop-casting process.[92] When Shao *et al.* evaporated M-CNC solution at 35 °C, a Maltese cross pattern emerged under the POM, which differs from the conventional cholesteric assembly structure. By mapping the linearly polarized FTIR signal of the film, they investigated the angular distribution of the M-CNCs, and Herman molecular orientation could be estimated, showing uniform alignment. The driving force behind the concentric alignment was identified through flow field characterization, particle image tracking, and finite element simulations, which showed a balance between the Marangoni flow and the capillary flow.

Based on the strategies for circular alignment, topographical templates are introduced to make a two-dimensional structure in the CNC deposited film (Fig. 9d).[93] The CNCs–PVA composite could be designed as a beautiful structure based on controlling the surface tension gradient on the embossed

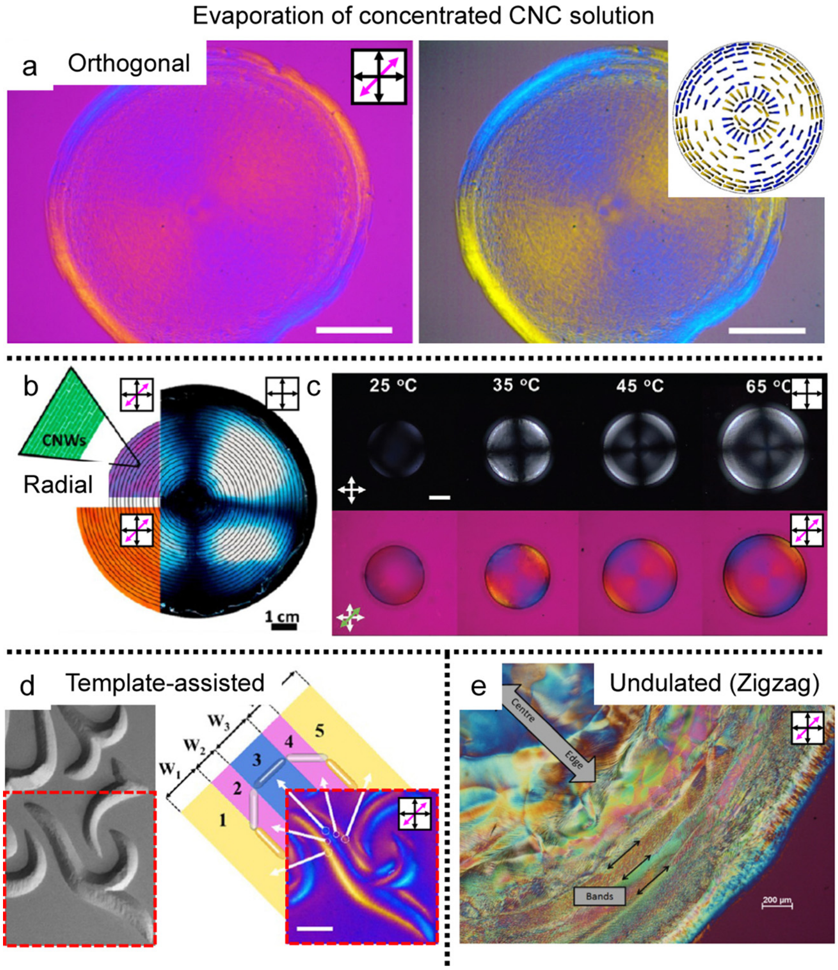

Fig. 9 Multiple morphologies of CNCs in the deposited film. (a) Orthogonal alignment in the dried sessile droplet. The right images were enhanced to highlight the blue and yellow regions which are indicative of CNC alignment. (b) and (c) Circular alignment of the CNCs in the deposited film induced by (b) additives and (c) surface modification. (d) Template-assisted two-dimensional structure of the CNCs and (e) cholesteric-induced periodic band structure. (a) Reproduced from ref. 87 with permission from Elsevier, copyright 2021. (b) Reproduced from ref. 88 with permission from American Chemical Society, copyright 2014. (c) Reproduced from ref. 92 with permission from John Wiley and Sons, copyright 2021. (d) Reproduced from ref. 89 with permission from American Chemical Society, copyright 2019. (e) Reproduced from ref. 23 with permission from MDPI, copyright 2015.

pattern. The M-CNCs forming the full concentric alignment in the sessile droplet formed various structures that the contact lines fixed by the template determine the alignment of the M-CNCs, which induces surface tension gradients depending on their shape. The demonstration suggested the possibility of tuning the birefringence pattern by changing the template's shape from symmetrical to asymmetrical and the array structure.

Last, Gray *et al.* initially found different alignments of CNC films in sessile droplet deposits (Fig. 9e).[24] They observed that fingerprint textures can be distorted by the flow of CNC liquid crystals in capillaries and found concentric alignments, helicoidal, and chiral multi-domain structures depending on the initial concentration and evaporation rate of the CNC dispersion. In particular, one kind of multi-domain, periodic radial band texture could be obtained by the distorted cholesteric phase of CNC. And they suggest that stick-and-slip behavior could also appear due to the anisotropic shrinkage of liquid crystals. Interestingly, the thickness difference induced by the stick-and-slip behavior was consistent with the half-pitch of the cholesteric phase. The researchers noted that their model was an oversimplification but significant in that they found a distorted fingerprint texture in the deposition process.

3.3. Protein amyloid

Amyloid fibrils are anisotropic colloids formed by self-assembly of peptide β-sheet aggregates into twisted and helical ribbons,[94,95] which have been intensely investigated in biology and medicine due to their relationship with pathological conditions such as age-related dementia (Fig. 10a).[96–98] The fibrillated proteins based on the amyloid core structure have recently been discovered at the origin of biological functionality in a remarkably diverse set of roles based on the unique properties and rich chemistry of peptides.[99,100]

The rod-like shape with the one-sided handedness induces isotropic to liquid crystal phase transition that can be well described by the Onsager theory extended to the charged and

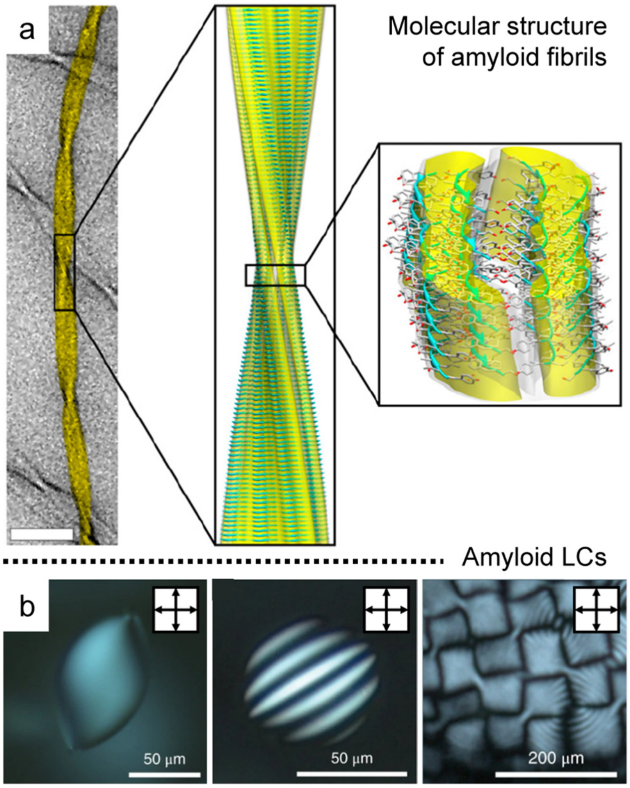

Fig. 10 Hierarchical anisotropy of protein amyloids. (a) Molecular structure of amyloid fibrils (b) a series of POM images in concentrated dispersion of amyloids; homogeneous nematic tactoid (left), uniaxial cholesteric tactoid (middle), and cholesteric focal conic domains (right). (a) Reproduced from ref. 94 with permission from The National Academy of Sciences, copyright 2013. (b) Reproduced from ref. 102 with permission from Springer Nature, copyright 2018.

semiflexible polymers, where modifying the system makes rich behavior in the concentrated solution (Fig. 10b).[26,101–103] In particular, Mezzenga *et al.* discovered the formation of tactoids along a concentration gradient, such as homogeneous, bipolar, and cholesteric ones, and analyzed the order and orientation transition in a confinement effect and hydrodynamic system with a support of theoretical estimation.[104–107]

For example, Almohammadi *et al.* investigated the liquid–liquid crystalline phase separation of aqueous filamentous colloids (here, beta-lactoglobulin amyloid fibrils) during droplet evaporation (Fig. 11a).[108] They demonstrated that two phase transitions occur with increasing concentration: nucleation and growth and spinodal decomposition where they also discovered the structural changes and dynamics of the tactoids in a hydrodynamic system. The amyloid alignment in the deposited films lacked macroscopic uniformity but retained hierarchical structures such as microscopic fingerprint textures and parabolic focal conic domains. It is similar to the CNCs' collective behavior in the drying process, including tactoid fusion close to the contact line with sliding instability or parabolic multi-domains in slow evaporation.

Our group reported, in collaboration with Mezzenga's group, the fabrication of a hierarchical structure of protein amyloids with the property of minimizing liquid crystal elastic energy in the vicinity of contact lines and a template capable of inducing stick-and-slip motion (Fig. 11b).[109] The filamentous protein amyloids self-assembled, while the contact line was pinned to form a macroscopic fibre structure, aligned parallel to the contact line, with micrometre-scale gaps along the edges that could be next pinned. A series of time-lapse POM images characterised the self-assembly process to elucidate the formation mechanism, and the structures' dimensions could also be controlled by adjusting the spacing of the templates.

3.4. Filamentous virus

The basic principles governing the isotropic-to-nematic phase transition in hard rods were established in the 1940s, focusing on the interplay of the aspect ratio and concentration.[35] In general, the properties of biopolymers are more complex than those of theoretical models, for example, due to flexibility and surface charge. However, Ff phages, a group of filamentous bacteriophage, have filled the gap with their molecular properties. For example, M13 phages have a contour length of 880 nm and a diameter of 6.6 nm, and their aspect ratio aligns with the Onsager criteria ($L/D > 100$) (Fig. 12a).[110] And the phages maintain the uniform conformation of length, topography, and chemical composition, yielding remarkably consistent suspensions. The capacity for tunability *via* chemical and biological methods enables systematic manipulation of interaction potentials,[111] rendering these models exceptionally effective for comprehending and designing liquid crystals. Consequently, these models facilitate direct quantitative comparisons with theoretical predictions, thereby facilitating investigations into intricate LC phases.[112–117] Noteworthy is the profound influence of molecular-level chirality on the self-assembly process within concentrated solutions. Leveraging insights, such as the formation of a helicoidal structure involving approximately 2700 copies of a single peptide and a fivefold rotation axis, researchers strive to comprehensively explore the origin and behavior of chiral mesophases, including cholesteric and chiral smectic C phases (Fig. 12b and c). The intricate relationship between microscopic and macroscopic chirality, encompassing factors like handedness and pitch, remains an ongoing focus of research, crucial for achieving a comprehensive understanding of colloidal liquid crystals.

Professor Belcher and Lee are pioneering researchers who have significantly contributed to fabricating functional materials using evaporation-induced self-assembly involving viral films.[118] Among their key findings, they have observed the formation of liquid crystal structures ranging from nematic to chiral smectic C, dependent on concentration and thickness variations.[119] At higher initial concentrations, the monodispersity of the bacteriophage led to the formation of helical bundles with a smectic-based long-range order, which is directly reflected in the film as a periodic zigzag structure. The authors attributed this phenomenon to the dominant effect of expressing chiral liquid crystal structures over the interfacial effect. AFM and laser diffraction pattern results with POM supported their assertion.

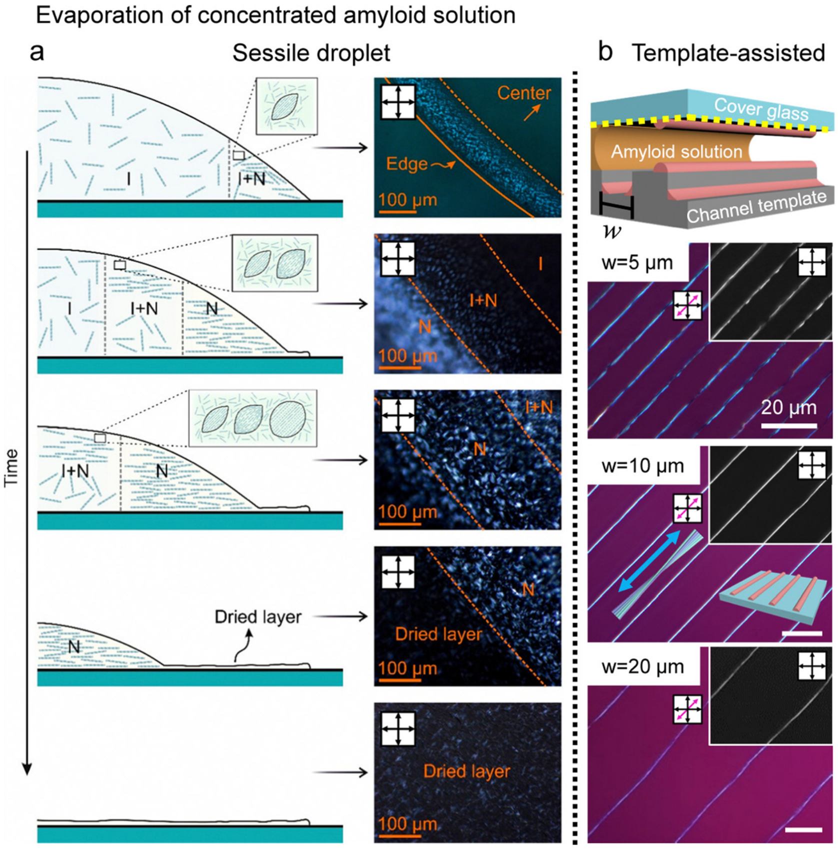

Fig. 11 Drying and deposition processes of the amyloid fibrils (a) real-time observation of the drying process of amyloid sessile droplets. (b) Hierarchical structure of amyloid fibrils induced by the microchannel template. White bars represent 20 µm. (a) Reproduced from ref. 108 with permission from American Chemical Society, copyright 2023. (b) Reproduced from ref. 109 with permission from American Chemical Society, copyright 2021.

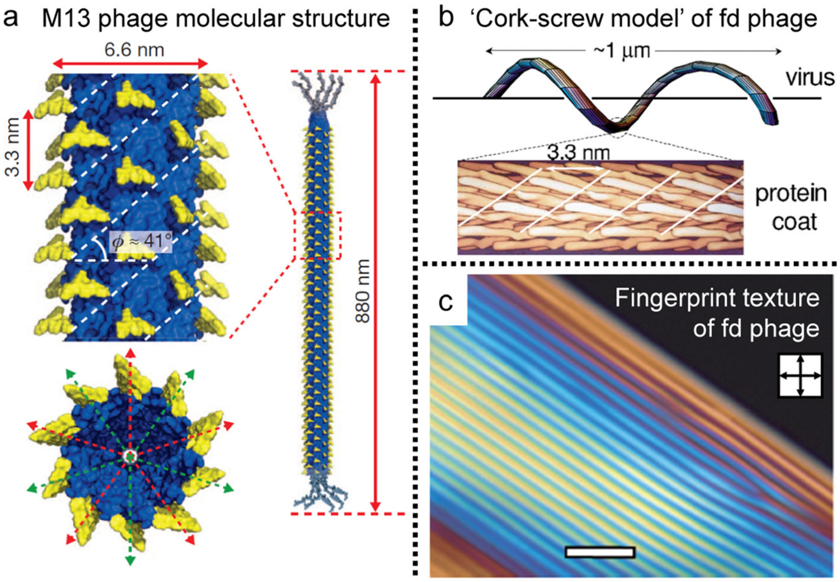

Fig. 12 Filamentous bacteriophages and their anisotropy. (a) Molecular structure of the M13 bacteriophage. (b) Schematic illustration of 'cork-screw model' of *fd* virus. (c) Cholesteric phase of concentrated viral solution exhibiting fingerprint texture under POM. (a) Reproduced from ref. 120 with permission from Springer Nature, copyright 2011. (b) Reproduced from ref. 115 with permission from American Physical Society, copyright 2003. (c) Reproduced from ref. 117 with permission from Royal Society of Chemistry, copyright 2009.

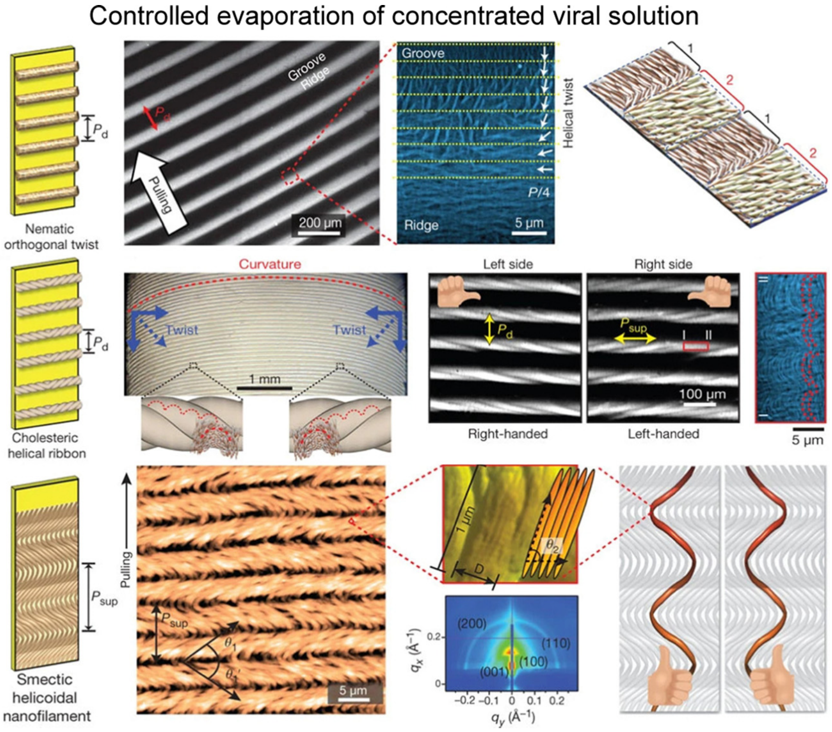

Fig. 13 Filamentous bacteriophage self-assembly. Film morphologies of M13 bacteriophage films; nematic orthogonal twist (first row), cholesteric helical ribbon (second row), and smectic helicoidal nanofilament (third row). The figure is reproduced from ref. 120 with permission from Springer Nature, copyright 2011.

Furthermore, the investigation by Lee and colleagues delved into the intricate interplay between environmental parameters and the kinetics governing the conversion of helical macromolecules into higher-ordered structures *via* a dip-coating process.[120,121] They explored the applicability of these factors for regulating assembly under controlled experimental conditions. Their study revealed that the formation of sub-micrometre-scale structures originated from the spontaneous transitions within liquid crystal dynamics, coupled with distinctive chiral characteristics, including nematic orthogonal twist, cholesteric helical ribbon, and smectic helicoidal nanofilament (Fig. 13). Examining at the microscale, the establishment of ordered configurations were closely tied to the geometric constraints such as curved menisci, along with the periodic modulation of material flow. By manipulating meniscus motion, they materialized the large-scale ordered film as a functional material. Moreover, by fine-tuning coating parameters within the self-assembly process, they successfully produced a diverse array of nanostructures on a large scale.[122] This achievement was facilitated by manipulating interparticle interactions contingent upon the concentration of additive ions. Adjustments to thermodynamic parameters resulted in distinctive undulations in the transient meniscus curve, leading to a hierarchical dotted pattern. Notably, the periodic alteration of coating speed, a pivot of kinetic factor, governed the formation of periodic dots within this pattern. Building on the groundwork, our group explored collective behaviors in non-equilibrium systems.[123] We focused on understanding the interplay between liquid crystal phase transition near the solution contact line and the resulting M13 film morphologies. Through multiple viewpoints of microscopic analysis, we directly visualized the presence of liquid crystal three-dimensional structures in the deposited films. We also involved the rheological and hydrodynamic analysis, revealing the competition between the liquid crystal elasticity and the capillary flows in forming hierarchical structures. Our work holds significance in optimizing experimental conditions for precise ordering and orientation of chiral filamentous colloids. By delving into the dynamics of non-equilibrium systems, we contribute to understanding intricate processes in this field.

3.5. Collagen fibril

In biological tissues, collagen fibrils are found in a highly concentrated state within the organic matrix of skeletal structures (Fig. 14a).[124–126] These fibrils endow specific properties, such as mechanical resistance in bones and tendons and transparency in the cornea.[127,128] The challenges in investigating these distinct properties within our tissues are rooted not only in the inherent attributes of the fibrils themselves but also in the hierarchical structure, spanning from the nanoscale to the microstructural level.[129] This spontaneous organization of well-ordered structures in diverse collagen matrices exhibits notable analogies to the liquid crystal ordering in the concentrated collagen solutions (Fig. 14b).[54,130–133]

The synthesis of collagen fibrils occurs within the cells, yielding three polypeptide chains that intertwin into an elongated,[134] semi-flexible triple helix with a diameter of 1.5 nm and a length of

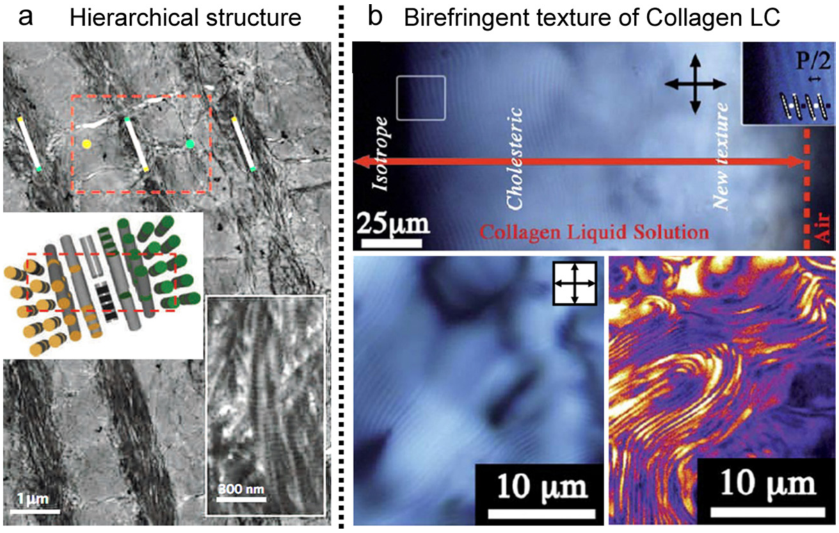

Fig. 14 Collagen LC structures. (a) Demineralized osteon in human compact bone (b) cholesteric fingerprint texture of collagen LCs in POM and a second harmonic generation microscope. (a) Reproduced from ref. 132 with permission from Springer Nature, copyright 2012. (b) Reproduced from ref. 120 with permission from Royal Society of Chemistry, copyright 2011.

300 nm. Due to the high aspect ratio, they presented lyotropic liquid crystal characteristics manifesting birefringent textures known as fingerprints above certain concentrations.[125,128,131] Early observations of these mesoscopic phases have been systematically clarified through joint endeavors by biologists and physicists aiming to quantitatively characterize collagen phase diagrams changing factors such as contour length, pH, ionic strength, solvent composition, and additives.[131] This foundational understanding has paved the way to modulate the long-range organization of collagen, enabling the establishment of uniaxial fibril orientations in tendons and layered orthogonal alignment in bone and the cornea and bridging the gap between *in vitro* findings and living tissues.

Trials to fabricate a biomimetic structure have been initiated since the 1980s through evaporating droplets containing collagen solutions (Fig. 15).[25,135–138] The surface morphologies of the resulting films are also quite similar in nature, and the researchers have analysed several key factors, including the initial concentration of the solution, as well as the dimensions (diameter and length) of the fibrils and the rate of evaporation.

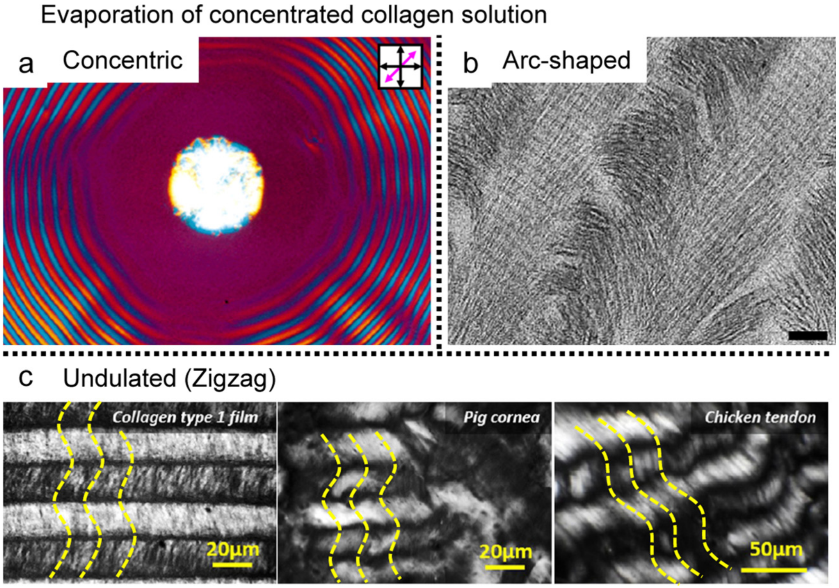

Fig. 15 Evaporation-induced self-assembly of collagen type 1. (a) Concentric ring pattern, (b) periodic arc-shaped, and (c) tissue-like ordered fibrillar network in the deposited collagen film. Yellow dashed lines represent the director of collagen. (a) Reproduced from ref. 135 with permission from American Chemical Society, copyright 1999. (b) Reproduced from ref. 24 with permission from Elsevier, copyright 2008. (c) Reproduced from ref. 138 with permission from American Chemical Society, copyright 2016.

For instance, Maeda conducted investigations utilizing techniques such as atomic force microscopy and polarized light microscopy (Fig. 15a).[135] This study highlighted the presence of a critical concentration threshold for nanoscale self-assembly. At concentrations below 0.005 mg mL^{-1}, collagen fibrils exhibited a random configuration on the mica substrate due to their inherent flexibility. However, as the initial concentration exceeded 0.05 mg ml^{-1}, these fibrils adopted a distinctive wavy crimp morphology characterized by periodic blue and yellow bands in polarized light microscopy. Within each band, the fibrils are uniaxially aligned and, at certain points, present interlocking and translational dislocation of these bands in the formation of concentric ring patterns.

Moreover, the diameter of the fibrils emerged as another crucial determinant of morphologies that varied based on solution pH (controlled by acetic acid) and the specific collagen types formed through natural fibrillogenesis.[137] These phenomena indirectly support the notion that the established collagen structures originated from liquid crystal-mediated self-assembly.[131] The application of a solution coating technique greatly enhanced the uniformity of the aligned collagen fibril network (Fig. 15b and c).[25,138] By precisely manipulating external variables, researchers successfully achieved a structure analogous to human connective tissue. The resultant structures, driven by liquid crystals, featured diverse hierarchical levels, such as the periodicity of the twisted plywood structure, upon the specific conditions applied.

Furthermore, professor Rey's group embarked on a theoretical exploration of the chiral self-assembly mechanism inherent to collagen I within a non-equilibrium system grounded in relaxation and transport principles.[139,140] The investigation demonstrated the pivotal role played by the simultaneous integration of isotropic-cholesteric phase ordering and anisotropic solvent transport in forming the helicoidal plywood structure. By simulating a biomimetic deposition process followed by controlled drying, it will be possible to finely regulate the hierarchical dimensions of the collagen structure.

4. Potential for practical applications

The alignment of building blocks in the deposited film can impart anisotropic characteristics to other materials, influenced by the surface morphology and the excluded volume effect of

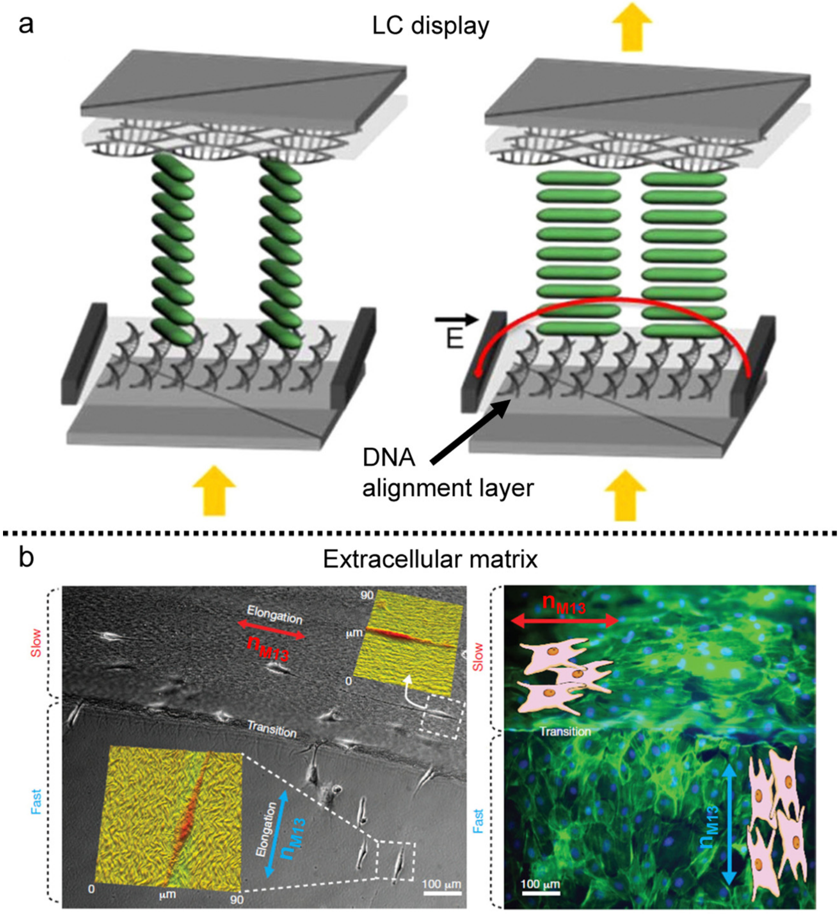

Fig. 16 Anisotropy transfer on the deposited film. (a) In-plane switching LC display using the DNA alignment layer. (b) Preosteoblast cell alignment on the mineralized bacteriophage film. n_{M13} represents the direction of M13 bacteriophages. (a) Reproduced from ref. 145 with permission from American Chemical Society, copyright 2015. (b) Reproduced from ref. 120 with permission from Springer Nature, copyright 2011.

additives. We will now present two illustrative applications of biopolymeric films: (i) as an alignment layer (Fig. 16) and (ii) as an anisotropic matrix (Fig. 17 and 18).

4.1. On the film: alignment layer

An alignment layer serves the purpose of inducing uniform and planar alignment of anisotropic entities such as molecules, polymer chains, inorganic rod-like particles, and even living matter near the surface. Its role is to exert control over the orientation and arrangement of these entities, enabling users to tailor their properties on the substrate. Various mechanisms drive alignment layers, including surface roughness, geometrical confinement, and chemical heterogeneity.[141,142] In this context, films produced using anisotropic biopolymers find application as alignment layers based on the anisotropy of those factors.

Similar to other alignment layers, these biopolymeric films not only align materials following the director on the deposited film but also induce tilted alignment based on molecular characteristics. For instance, DNA, with its ability to induce tilted alignment relative to the long axis of its chains,[143] can serve as an alignment layer for thermotropic liquid crystals (Fig. 16a).[144,145] The DNA LC solution is coatable and can be applied as the alignment layer without a rubbing process due to the grooves in the chains. Sandwiched cells composed of a DNA alignment layer and thermotropic LCs could be employed in twisted-nematic and in-plane switching displays.

Furthermore, biomolecular alignment layers extend beyond nanomaterials, finding utility in cell alignment and tissue engineering due to their inherent biocompatibility (Fig. 17b). The layers immobilized by chemical treatment can be applied to an extracellular matrix that can align cellular structures on the surface.[120,138] These templates introduce anisotropic mechanical stresses during cellular differentiation and migration processes, and precise control over surface grooves *via* coating processes enables diverse cell alignments on dried films. The controllability based on LC elastic behavior would provide various topographic bio-templates for tissue scaffolding.

4.2. In the film: anisotropic matrix

The fluidity of liquid crystals enables them to function as solvents when mixed with additives, while their crystalline nature imparts directional alignment to these additives. This alignment in the liquid crystal medium is primarily driven by entropic steric interactions, which seek to maximize translational entropy at the expense of rotational entropy, a phenomenon initially described

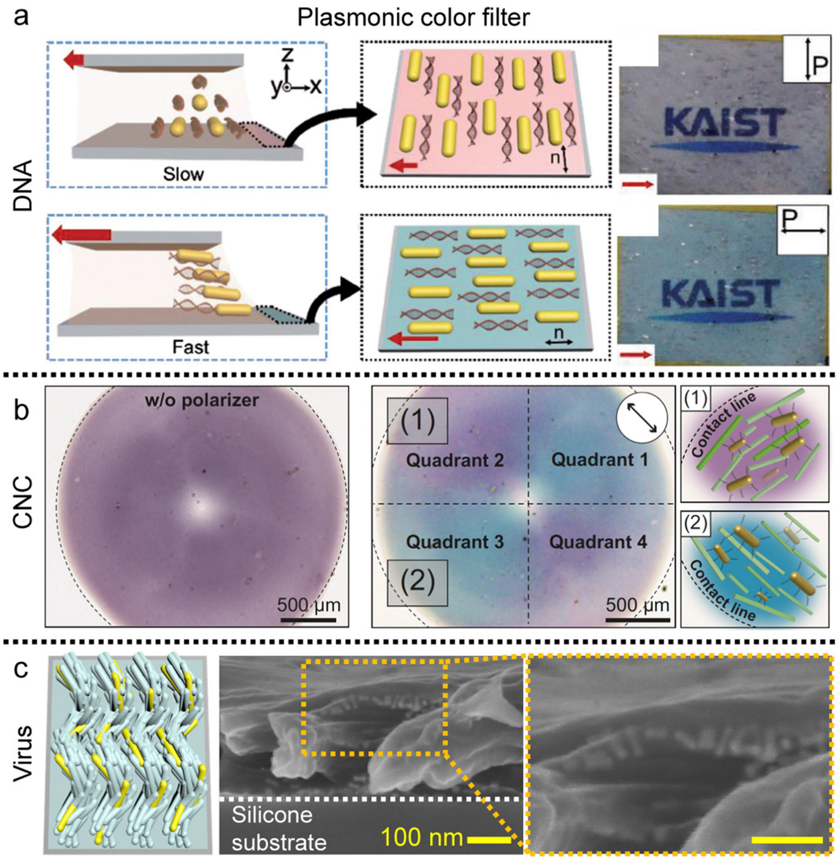

Fig. 17 Alignment of metal nanorods in the anisotropic matrix. (a) Uniaxial gold nanorod arrangement in the DNA matrix and (b) concentric alignment of nanorods in the circular CNC film. Plasmonic color is changed by the direction of the single polarizer. (c) Helicoidal nanorod alignment in the viral film. (a) Reproduced from ref. 72 with permission from John Wiley and Sons, copyright 2017. (b) Reproduced from ref. 91 with permission from Springer Nature, copyright 2023. (c) Reproduced from ref. 123 with permission from John Wiley and Sons, copyright 2021.

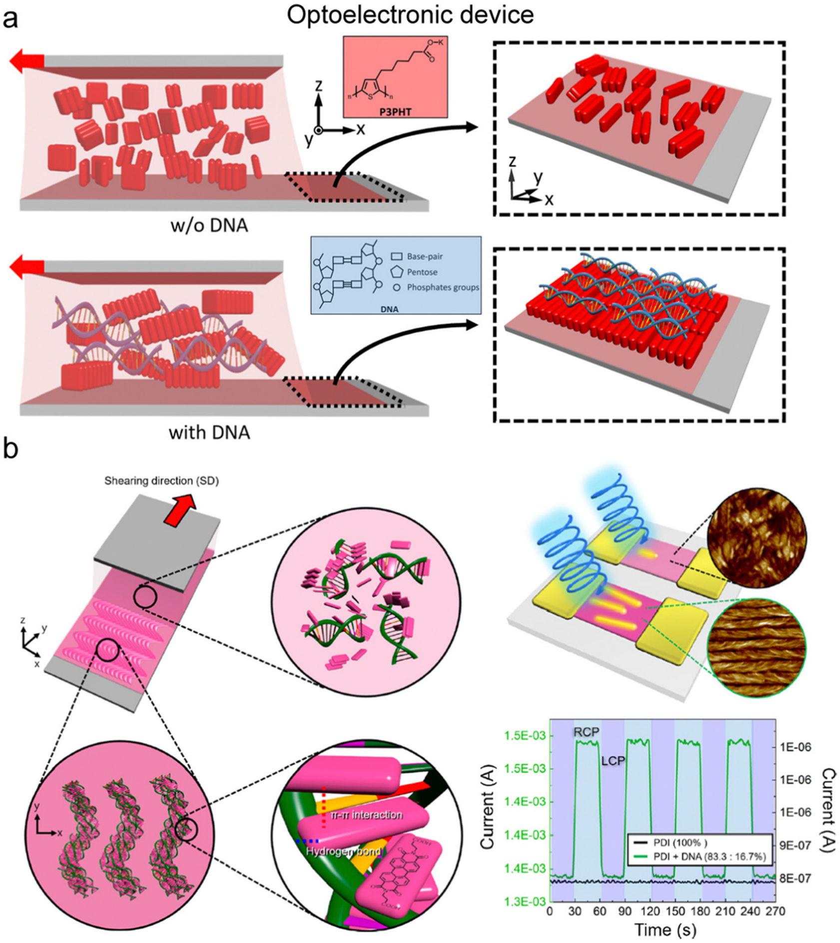

Fig. 18 Control of electron transfer in the aligned matrix. (a) Enhancement of conducting polymer alignment by mixing with DNA. In the illustration, red blocks represent the conducting polymer, P3PHT, that is poly[3-(potassium-7-hexanoate)-thiophene-2,5-diyl]. (b) Helicoidal DNA-conjugated molecule composites and their chiral optoelectrical activity. (a) Reproduced from ref. 153 with permission from American Chemical Society, copyright 2020. (b) Reproduced from ref. 154 with permission from American Chemical Society, copyright 2021.

by Onsager.[35,146] The excluded volume effect, which tends to increase the effective volume of building blocks, not only facilitates the development of liquid crystal phases in concentrated solutions but also induces uniaxial alignment of the solutes along the local director of liquid crystals. The orientational ordering of solutes becomes arrested in the film after drying.

These findings demonstrate that co-dispersions allow for the alignment of nanorods with relatively small aspect ratios, which cannot spontaneously form ordered liquid crystal structures independently.[147–150] These nanorods are of particular interest due to their high surface-to-volume ratio and their responsiveness to optical, chemical, and electrical stimuli in an anisotropic manner.[151,152] Gold nanorods (GNRs), one of the examples, dispersed in a DNA solution exhibit various nematic-like ordering along with the local director of DNA chains (Fig. 17a).[73,74] The resulting DNA-GNR composite film displays polarization-dependent extinction colors based on localized surface plasmon resonance (LSPR). Additionally, the absorption spectrum of the films reveals that the longitudinal SPR peak is pronounced when the linearly polarized light aligns with the long axis of GNRs, whereas it becomes minimal when the polarizer is perpendicular. If the absorbance, including both longitudinal and transverse, is in the visible light range, the transmissive/reflective color can vary depending on the polarizer's angle.

Moreover, the GNRs formed a concentric pattern along the orientation of the CNCs in the deposited film. The GNRs dispersed in the CNCs are drop-cast on the flat substrate and the circular CNC-GNR film exhibited quadrant pattern under a single polarizer consisting of purple and blue colors along the orientation of the GNRs (Fig. 17b).[91]

Not only the two-dimensional structure, but the nanorods also form three-dimensional structures in the medium of chiral-induced liquid crystals (Fig. 17c).[123] Within viral films, nanorods form helicoidal structures, exhibiting axis-symmetric rotation with a specific azimuthal angle. This may serve as a coatable plasmonic optical filter with circular dichroism as the result of collective linear polarization effects.

Directional alignment within an anisotropic matrix also governs electrical properties. Water-soluble modifications of conducting polymers yield anisotropic structures when incorporated into a biopolymer medium during deposition, induced by controlled nucleation and growth, or during the drying process through phase separation (Fig. 18).[153,154] Thiophene-based polymers engage in dipole–dipole interactions with DNA phosphate groups and align under the DNA layer due to the molecular grooves of DNA (Fig. 18a).[153] The resulting composite demonstrates anisotropic electrical behavior in the part of an organic field-effect transistor (OFET), where electron or hole transport properties vary based on the interchain and intrachain direction. Furthermore, the electrical properties are regulated by the external optical stimuli in an anisotropic manner due to the aligned structure (Fig. 18b).[154] Perylene-based molecules intercalate between DNA base pairs through π–π interactions and form a helical structure in the solution coating process. The deposited film selectively interacts with the circularly polarized light displaying an ON/OFF behavior in the OFET device. These examples underscore the significant potential for further research on the application of anisotropic transfer induced by co-dispersion, coupled with other material characteristics.

Conclusions

In this review, we have presented current research findings regarding the self-assembly phenomena and deposition process of anisotropic biopolymers and colloids induced by evaporation (Table 1). Based on the Onsager theory, anisotropic biomaterials exhibiting a liquid crystalline phase above a specific concentration undergo a phase transition to a liquid crystalline state during the solution's evaporation. The resulting liquid crystalline structure is then mirrored in the deposited film during the deposition process. To comprehend the mechanisms governing the formation of these structures driven by the liquid crystal phase within the film and to exercise control over them through the solution process, extensive experimentation involving the manipulation of various parameters was conducted. Our approach aimed to advance the understanding of the formation mechanism by employing theoretical foundations comprehending the flow characteristics in evaporating solutions, polymer rheology, and the elastic properties of liquid crystal materials. Furthermore, recent report suggests the initial steps for practical applications of anisotropic biopolymers as fundamental building blocks,[170] aiming to enrich the material value of anisotropic biopolymers and unravel their distinctive behavior in confined, non-equilibrium systems.

Conflicts of interest

There are no conflicts to declare.

Acknowledgements

This work was supported by the National Research Foundation of Korea (NRF) grant funded by the Korean Government (MSIT) (RS-2023-00273025, 2021M3H4A3A01050378).

Notes and references

1 W. Brutsaert, *Evaporation into the atmosphere: theory, history and applications*, Springer Science & Business Media, 2013, vol. 1.
2 J. L. Monteith, *Q.J.R. Meteorol. Soc.*, 1981, **107**, 1–27.
3 T. P. Bigioni, X.-M. Lin, T. T. Nguyen, E. I. Corwin, T. A. Witten and H. M. Jaeger, *Nat. Mater.*, 2006, **5**, 265–270.
4 Y. Diao, B. C.-K. Tee, G. Giri, J. Xu, D. H. Kim, H. A. Becerril, R. M. Stoltenberg, T. H. Lee, G. Xue, S. C. B. Mannsfeld and Z. Bao, *Nat. Mater.*, 2013, **12**, 665–671.
5 H. Kim, F. Boulogne, E. Um, I. Jacobi, E. Button and H. A. Stone, *Phys. Rev. Lett.*, 2016, **116**, 124501.
6 W. Han and Z. Lin, *Angew. Chem., Int. Ed.*, 2012, **51**, 1534–1546.
7 D. J. Harris, H. Hu, J. C. Conrad and J. A. Lewis, *Phys. Rev. Lett.*, 2007, **98**, 148301.
8 R. D. Deegan, O. Bakajin, T. F. Dupont, G. Huber, S. R. Nagel and T. A. Witten, *Nature*, 1997, **389**, 827–829.
9 R. D. Deegan, O. Bakajin, T. F. Dupont, G. Huber, S. R. Nagel and T. A. Witten, *Phys. Rev. E: Stat. Phys., Plasmas, Fluids, Relat. Interdiscip. Top.*, 2000, **62**, 756–765.
10 D. Orejon, K. Sefiane and M. E. R. Shanahan, *Langmuir*, 2011, **27**, 12834–12843.
11 S. Maheshwari, L. Zhang, Y. Zhu and H.-C. Chang, *Phys. Rev. Lett.*, 2008, **100**, 044503.
12 P. J. Yunker, T. Still, M. A. Lohr and A. G. Yodh, *Nature*, 2011, **476**, 308–311.
13 P. J. Sáenz, A. W. Wray, Z. Che, O. K. Matar, P. Valluri, J. Kim and K. Sefiane, *Nat. Commun.*, 2017, **8**, 14783.
14 F. Girard, M. Antoni, S. Faure and A. Steinchen, *Colloids Surf., A*, 2008, **323**, 36–49.
15 K. Uno, K. Hayashi, T. Hayashi, K. Ito and H. Kitano, *Colloid Polym. Sci.*, 1998, **276**, 810–815.
16 H. Hu and R. G. Larson, *Langmuir*, 2005, **21**, 3972–3980.
17 Z. S. Davidson, Y. Huang, A. Gross, A. Martinez, T. Still, C. Zhou, P. J. Collings, R. D. Kamien and A. G. Yodh, *Nat. Commun.*, 2017, **8**, 15642.
18 A. D. Rey and E. E. Herrera-Valencia, *Biopolymers*, 2012, **97**, 374–396.
19 I. W. Hamley, *Soft Matter*, 2010, **6**, 1863–1871.
20 A. Bensimon, A. Simon, A. Chiffaudel, V. Croquette, F. Heslot and D. Bensimon, *Science*, 1994, **265**, 2096–2098.
21 D. Bensimon, A. J. Simon, V. Croquette and A. Bensimon, *Phys. Rev. Lett.*, 1995, **74**, 4754–4757.
22 N. Morii, G. Kido, H. Suzuki and H. Morii, *Biopolymers*, 2005, **77**, 163–172.
23 D. G. Gray and X. Mu, *Materials*, 2015, **8**, 7873–7888.
24 M.-M. Giraud-Guille, E. Belamie, G. Mosser, C. Helary, F. Gobeaux and S. Vigier, *C. R. Chim*, 2008, **11**, 245–252.
25 G. Nyström and R. Mezzenga, *Curr. Opin. Colloid Interface Sci.*, 2018, **38**, 30–44.
26 O. Reynolds, *Philos. Trans. R. Soc. London*, 1883, **174**, 935–982.
27 H. Gelderblom, C. Diddens and A. Marin, *Soft Matter*, 2022, **18**, 8535–8553.

28 A.-M. Cazabat and G. Guéna, *Soft Matter*, 2010, **6**, 2591.

29 M. He, B. Li, X. Cui, B. Jiang, Y. He, Y. Chen, D. O'Neil, P. Szymanski, M. A. EI-Sayed, J. Huang and Z. Lin, *Nat. Commun.*, 2017, **8**, 16045.

30 Y. Yu. Tarasevich, I. V. Vodolazskaya and O. P. Isakova, *Colloid Polym. Sci.*, 2011, **289**, 1015–1023.

31 M. Le Berre, Y. Chen and D. Baigl, *Langmuir*, 2009, **25**, 2554–2557.

32 G. Berteloot, C.-T. Pham, A. Daerr, F. Lequeux and L. Limat, *Europhys. Lett.*, 2008, **83**, 14003.

33 X. Gu, L. Shaw, K. Gu, M. F. Toney and Z. Bao, *Nat. Commun.*, 2018, **9**, 534.

34 L. Onsager, *Ann. N.Y. Acad. Sci.*, 1949, **51**, 627–659.

35 A. R. Khokhlov and A. N. Semenov, *Physica A*, 1981, **108**, 546–556.

36 S.-D. Lee and R. B. Meyer, *Phys. Rev. Lett.*, 1988, **61**, 2217–2220.

37 R. B. Meyer, F. Lonberg, V. Taratuta, S. Fraden, S.-D. Lee and A. J. Hurd, *Faraday Discuss. Chem. Soc.*, 1985, **79**, 125.

38 T. Odijk, *Macromolecules*, 1986, **19**, 2313–2329.

39 R. G. Priest, *Phys. Rev. A*, 1973, **7**, 720–729.

40 S. Onogi and T. Asada, in *Rheology*, ed. G. Astarita, G. Marrucci and L. Nicolais, Springer US, Boston, MA, 1980, pp. 127–147.

41 *Flowing Matter*, ed. F. Toschi and M. Sega, Springer International Publishing, Cham, 2019.

42 I. I. Smalyukh, O. V. Zribi, J. C. Butler, O. D. Lavrentovich and G. C. L. Wong, *Phys. Rev. Lett.*, 2006, **96**, 177801.

43 S. Zhou, Yu. A. Nastishin, M. M. Omelchenko, L. Tortora, V. G. Nazarenko, O. P. Boiko, T. Ostapenko, T. Hu, C. C. Almasan, S. N. Sprunt, J. T. Gleeson and O. D. Lavrentovich, *Phys. Rev. Lett.*, 2012, **109**, 037801.

44 S. Zhou, *Lyotropic Chromonic Liquid Crystals*, Springer International Publishing, Cham, 2017.

45 L. Lucchetti, T. P. Fraccia, G. Nava, T. Turiv, F. Ciciulla, L. Bethge, S. Klussmann, O. D. Lavrentovich and T. Bellini, *ACS Macro Lett.*, 2020, **9**, 1034–1039.

46 R. G. Larson and D. W. Mead, *Liq. Cryst.*, 1993, **15**, 151–169.

47 Y. J. Cha, M.-J. Gim, H. Ahn, T. J. Shin, J. Jeong and D. K. Yoon, *ACS Appl. Mater. Interfaces*, 2017, **9**, 18355–18361.

48 F. Livolant, *Physica A*, 1991, **176**, 117–137.

49 M. H. Chow, K. T. H. Yan, M. J. Bennett and J. T. Y. Wong, *Eukaryot. Cell*, 2010, **9**, 1577–1587.

50 D. Frenkiel-Krispin, *EMBO J.*, 2001, **20**, 1184–1191.

51 R. L. Rill, F. Livolant, H. C. Aldrich and M. W. Davidson, *Chromosoma*, 1989, **98**, 280–286.

52 P. Gouet, J. M. Diprose, J. M. Grimes, R. Malby, J. N. Burroughs, S. Zientara, D. I. Stuart and P. P. Mertens, *Cell*, 1999, **97**, 481–490.

53 F. Livolant, *Tissue Cell*, 1984, **16**, 535–555.

54 J. Roca, *Chromosoma*, 2011, **120**, 323–334.

55 M. T. J. Van Loenhout, M. V. De Grunt and C. Dekker, *Science*, 2012, **338**, 94–97.

56 S. Jones, H. P. Shanahan, H. M. Berman and J. M. Thornton, *Nucleic Acids Res.*, 2003, **31**, 7189–7198.

57 H. Cedar and Y. Bergman, *Nat. Rev. Genet.*, 2009, **10**, 295–304.

58 A. Minsky, E. Shimoni and D. Frenkiel-Krispin, *Nat. Rev. Mol. Cell Biol.*, 2002, **3**, 50–60.

59 R. E. Franklin and R. G. Gosling, *Nature*, 1953, **171**, 740–741.

60 J. D. Watson and F. H. Crick, *Nature*, 1953, **171**, 737–738.

61 F. Livolant, A. M. Levelut, J. Doucet and J. P. Benoit, *Nature*, 1989, **339**, 724–726.

62 R. L. Rill, *Proc. Natl. Acad. Sci. U. S. A.*, 1986, **83**, 342–346.

63 T. E. Strzelecka, M. W. Davidson and R. L. Rill, *Nature*, 1988, **331**, 457–460.

64 P. J. Hagerman, *Annu. Rev. Biophys. Biophys. Chem.*, 1988, **17**, 265–286.

65 M. Nakata, G. Zanchetta, B. D. Chapman, C. D. Jones, J. O. Cross, R. Pindak, T. Bellini and N. A. Clark, *Science*, 2007, **318**, 1276–1279.

66 E. S. Sobel and J. A. Harpst, *Biopolymers*, 1991, **31**, 1559–1564.

67 S. B. Smith, L. Finzi and C. Bustamante, *Science*, 1992, **258**, 1122–1126.

68 C. B. Stanley, H. Hong and H. H. Strey, *Biophys. J.*, 2005, **89**, 2552–2557.

69 F. Livolant and A. Leforestier, *Prog. Polym. Sci.*, 1996, **21**, 1115–1164.

70 S. H. Kang, W. S. Hwang, Z. Lin, S. H. Kwon and S. W. Hong, *Nano Lett.*, 2015, **15**, 7913–7920.

71 Y. J. Cha and D. K. Yoon, *Adv. Mater.*, 2017, **29**, 1604247.

72 Y. J. Cha, D. S. Kim and D. K. Yoon, *Adv. Funct. Mater.*, 2017, **27**, 1703790.

73 Y. J. Cha, S. M. Park, R. You, H. Kim and D. K. Yoon, *Nat. Commun.*, 2019, **10**, 2512.

74 S. M. Park, G. Park, Y. J. Cha and D. K. Yoon, *Small*, 2020, **16**, 2002449.

75 J. P. F. Lagerwall, C. Schütz, M. Salajkova, J. Noh, J. Hyun Park, G. Scalia and L. Bergström, *NPG Asia Mater.*, 2014, **6**, e80.

76 T. Li, C. Chen, A. H. Brozena, J. Y. Zhu, L. Xu, C. Driemeier, J. Dai, O. J. Rojas, A. Isogai, L. Wågberg and L. Hu, *Nature*, 2021, **590**, 47–56.

77 I. I. Smalyukh, *Adv. Mater.*, 2021, **33**, 2001228.

78 S. J. Eichhorn, A. Etale, J. Wang, L. A. Berglund, Y. Li, Y. Cai, C. Chen, E. D. Cranston, M. A. Johns, Z. Fang, G. Li, L. Hu, M. Khandelwal, K.-Y. Lee, K. Oksman, S. Pinitsoontorn, F. Quero, A. Sebastian, M. M. Titirici, Z. Xu, S. Vignolini and B. Frka-Petesic, *J. Mater. Sci.*, 2022, **57**, 5697–5767.

79 D. Klemm, F. Kramer, S. Moritz, T. Lindström, M. Ankerfors, D. Gray and A. Dorris, *Angew. Chem., Int. Ed.*, 2011, **50**, 5438–5466.

80 E. Kontturi, P. Laaksonen, M. B. Linder Nonappa, A. H. Gröschel, O. J. Rojas and O. Ikkala, *Adv. Mater.*, 2018, **30**, 1703779.

81 R. M. Parker, G. Guidetti, C. A. Williams, T. Zhao, A. Narkevicius, S. Vignolini and B. Frka-Petesic, *Adv. Mater.*, 2018, **30**, 1704477.

82 Y. Ogawa, *Nanoscale*, 2019, **11**, 21767.

83 P.-X. Wang, W. Y. Hamad and M. J. MacLachlan, *Nat. Commun.*, 2016, **7**, 11515.

84 Y. Geng, R. Kizhakidathazhath and J. P. Lagerwall, *Nat. Mater.*, 2022, **21**, 1441–1447.

85 B. E. Droguet, H.-L. Liang, B. Frka-Petesic, R. M. Parker, M. F. De Volder, J. J. Baumberg and S. Vignolini, *Nat. Mater.*, 2022, **21**, 352–358.

86 A. Tran, C. E. Boott and M. J. MacLachlan, *Adv. Mater.*, 2020, **32**, 1905876.

87 C. Q. Pritchard, F. Navarro, M. Roman and M. J. Bortner, *J. Colloid Interface Sci.*, 2021, **603**, 450–458.

88 M. Mashkour, T. Kimura, F. Kimura, M. Mashkour and M. Tajvidi, *Biomacromolecules*, 2014, **15**, 60–65.

89 M. Mashkour, T. Kimura, M. Mashkour, F. Kimura and M. Tajvidi, *ACS Appl. Mater. Interfaces*, 2019, **11**, 1538–1545.

90 M. Talantikite, N. Leray, S. Durand, C. Moreau and B. Cathala, *J. Colloid Interface Sci.*, 2021, **587**, 727–735.

91 J. Pyeon, S. M. Park, J. Kim, J.-H. Kim, Y.-J. Yoon, D. K. Yoon and H. Kim, *Nat. Commun.*, 2023, **14**, 8096.

92 R. Shao, X. Meng, Z. Shi, J. Zhong, Z. Cai, J. Hu, X. Wang, G. Chen, S. Gao, Y. Song and C. Ye, *Small Methods*, 2021, **5**, 2100690.

93 H. Wang, R. Shao, X. Meng, Y. He, Z. Shi, Z. Guo and C. Ye, *ACS Appl. Mater. Interfaces*, 2022, **14**, 36277–36286.

94 A. W. P. Fitzpatrick, G. T. Debelouchina, M. J. Bayro, D. K. Clare, M. A. Caporini, V. S. Bajaj, C. P. Jaroniec, L. Wang, V. Ladizhansky, S. A. Müller, C. E. MacPhee, C. A. Waudby, H. R. Mott, A. De Simone, T. P. J. Knowles, H. R. Saibil, M. Vendruscolo, E. V. Orlova, R. G. Griffin and C. M. Dobson, *Proc. Natl. Acad. Sci. U. S. A.*, 2013, **110**, 5468–5473.

95 M. G. Iadanza, M. P. Jackson, E. W. Hewitt, N. A. Ranson and S. E. Radford, *Nat. Rev. Mol. Cell Biol.*, 2018, **19**, 755–773.

96 F. Chiti and C. M. Dobson, *Annu. Rev. Biochem.*, 2006, **75**, 333–366.

97 D. Eisenberg and M. Jucker, *Cell*, 2012, **148**, 1188–1203.

98 T. P. Knowles, M. Vendruscolo and C. M. Dobson, *Nat. Rev. Mol. Cell Biol.*, 2014, **15**, 384–396.

99 T. P. J. Knowles and R. Mezzenga, *Adv. Mater.*, 2016, **28**, 6546–6561.

100 P. C. Ke, R. Zhou, L. C. Serpell, R. Riek, T. P. J. Knowles, H. A. Lashuel, E. Gazit, I. W. Hamley, T. P. Davis, M. Fändrich, D. E. Otzen, M. R. Chapman, C. M. Dobson, D. S. Eisenberg and R. Mezzenga, *Chem. Soc. Rev.*, 2020, **49**, 5473–5509.

101 A. M. Corrigan, C. Müller and M. R. H. Krebs, *J. Am. Chem. Soc.*, 2006, **128**, 14740–14741.

102 G. Nyström, M. Arcari and R. Mezzenga, *Nat. Nanotechnol.*, 2018, **13**, 330–336.

103 M. Bagnani, G. Nyström, C. De Michele and R. Mezzenga, *ACS Nano*, 2019, **13**, 591–600.

104 S. A. Khadem, M. Bagnani, R. Mezzenga and A. D. Rey, *Nat. Commun.*, 2020, **11**, 4616.

105 H. Almohammadi, M. Bagnani and R. Mezzenga, *Nat. Commun.*, 2020, **11**, 5416.

106 H. Almohammadi, S. Martinek, Y. Yuan, P. Fischer and R. Mezzenga, *Nat. Commun.*, 2023, **14**, 607.

107 P. Azzari and R. Mezzenga, *Phys. Rev. Res.*, 2023, **5**, 013137.

108 H. Almohammadi, Y. Fu and R. Mezzenga, *ACS Nano*, 2023, **17**, 3098–3106.

109 S. M. Park, M. Bagnani, H. S. Yun, M. J. Han, R. Mezzenga and D. K. Yoon, *ACS Nano*, 2021, **15**, 20261–20266.

110 *Soft Matter*, ed. G. Gompper and M. Schick, Wiley-VCH Verlag GmbH & Co. KGaA, Weinheim, Germany, vol. 2, 2005.

111 S. Y. Yoo, W.-J. Chung and D.-Y. Lee, *Int. J. Nanores.*, 2014, 5825.

112 Z. Dogic and S. Fraden, *Phys. Rev. Lett.*, 1997, **78**, 2417–2420.

113 L. C. Welsh, M. F. Symmons, C. Nave, R. N. Perham, E. A. Marseglia and D. A. Marvin, *Macromolecules*, 1996, **29**, 7075–7083.

114 Z. Dogic and S. Fraden, *Langmuir*, 2000, **16**, 7820–7824.

115 E. Grelet and S. Fraden, *Phys. Rev. Lett.*, 2003, **90**, 198302.

116 Z. Zhang, N. Krishna, M. P. Lettinga, J. Vermant and E. Grelet, *Langmuir*, 2009, **25**, 2437–2442.

117 E. Barry, D. Beller and Z. Dogic, *Soft Matter*, 2009, **5**, 2563–2570.

118 J. H. Lee, C. M. Warner, H.-E. Jin, E. Barnes, A. R. Poda, E. J. Perkins and S.-W. Lee, *Nat. Protoc.*, 2017, **12**, 1999–2013.

119 S.-W. Lee, B. M. Wood and A. M. Belcher, *Langmuir*, 2003, **19**, 1592–1598.

120 W.-J. Chung, J.-W. Oh, K. Kwak, B. Y. Lee, J. Meyer, E. Wang, A. Hexemer and S.-W. Lee, *Nature*, 2011, **478**, 364–368.

121 J.-W. Oh, W.-J. Chung, K. Heo, H.-E. Jin, B. Y. Lee, E. Wang, C. Zueger, W. Wong, J. Meyer, C. Kim, S.-Y. Lee, W.-G. Kim, M. Zemla, M. Auer, A. Hexemer and S.-W. Lee, *Nat. Commun.*, 2014, **5**, 3043.

122 K. Heo, H.-E. Jin, H. Kim, J. H. Lee, E. Wang and S.-W. Lee, *Nano Energy*, 2019, **56**, 716–723.

123 S. M. Park, W. Kim, J. Kim, E. Choi, H. Kim, J. Oh and D. K. Yoon, *Small*, 2021, **17**, 2008097.

124 D. W. L. Hukins and J. Woodhead-galloway, *Mol. Cryst. Liq. Cryst.*, 1977, **41**, 33–39.

125 M.-M. Giraud-Guille, *J. Mol. Biol.*, 1992, **224**, 861–873.

126 F. Gobeaux, E. Belamie, G. Mosser, P. Davidson, P. Panine and M.-M. Giraud-Guille, *Langmuir*, 2007, **23**, 6411–6417.

127 D. W. L. Hukins, *J. Theo. Biol.*, 1978, **71**, 661–667.

128 M. M. Giraud-Guille, G. Mosser and E. Belamie, *Curr. Opin. Colloid Interface Sci.*, 2008, **13**, 303–313.

129 C. Sanchez, H. Arribart and M. M. Giraud Guille, *Nat. Mater.*, 2005, **4**, 277–288.

130 M.-M. Giraud-guille, *Mol. Cryst. Liq. Cryst.*, 1987, **153**, 15–30.

131 P. De Sa Peixoto, A. Deniset-Besseau, M.-C. Schanne-Klein and G. Mosser, *Soft Matter*, 2011, **7**, 11203.

132 Y. Wang, T. Azaïs, M. Robin, A. Vallée, C. Catania, P. Legriel, G. Pehau-Arnaudet, F. Babonneau, M.-M. Giraud-Guille and N. Nassif, *Nat. Mater.*, 2012, **11**, 724–733.

133 A. I. Brown, L. Kreplak and A. D. Rutenberg, *Soft Matter*, 2014, **10**, 8500–8511.

134 K. E. Kadler, D. F. Holmes, J. A. Trotter and J. A. Chapman, *Biochem. J.*, 1996, **316**, 1–11.

135 H. Maeda, *Langmuir*, 1999, **15**, 8505–8513.

136 J. E. Kirkwood and G. G. Fuller, *Langmuir*, 2009, **25**, 3200–3206.

137 L. Muthusubramaniam, L. Peng, T. Zaitseva, M. Paukshto, G. R. Martin and T. A. Desai, *J. Biomed. Mater. Res.*, 2012, **100A**, 613–621.

138 J. C. Price, P. Roach and A. J. El Haj, *ACS Biomater. Sci. Eng.*, 2016, **2**, 625–633.

139 O. F. Aguilar Gutierrez and A. D. Rey, *Soft Matter*, 2017, **13**, 8076–8088.

140 S. A. Khadem and A. D. Rey, *Front. Phys.*, 2019, **7**, 88.

141 J. Hoogboom, T. Rasing, A. E. Rowan and R. J. M. Nolte, *J. Mater. Chem.*, 2006, **16**, 1305–1314.

142 M. J. Shin and D. K. Yoon, *Materials*, 2020, **13**, 5466.

143 M. Nakata, G. Zanchetta, M. Buscaglia, T. Bellini and N. A. Clark, *Langmuir*, 2008, **24**, 10390–10394.

144 Y. J. Cha, M.-J. Gim, K. Oh and D. K. Yoon, *J. Inf. Disp.*, 2015, **16**, 129–135.

145 Y. J. Cha, M.-J. Gim, K. Oh and D. K. Yoon, *ACS Appl. Mater. Interfaces*, 2015, **7**, 13627–13632.

146 Q. Liu, M. G. Campbell, J. S. Evans and I. I. Smalyukh, *Adv. Mater.*, 2014, **26**, 7178–7184.

147 A. Querejeta-Fernández, G. Chauve, M. Methot, J. Bouchard and E. Kumacheva, *J. Am. Chem. Soc.*, 2014, **136**, 4788–4793.

148 J. V. Rie, G. González-Rubio, S. Kumar, C. Schütz, J. Kohlbrecher, M. Vanroelen, T. V. Gerven, O. Deschaume, C. Bartic, L. M. Liz-Marzán, G. Salazar-Alvarez and W. Thielemans, *Chem. Commun.*, 2020, **56**, 13001–13004.

149 Z. Cheng, Y. Ma, L. Yang, F. Cheng, Z. Huang, A. Natan, H. Li, Y. Chen, D. Cao, Z. Huang, Y. Wang, Y. Liu, R. Yang and H. Zhu, *Adv. Opt. Mater.*, 2019, **7**, 1801816.

150 Y. Yuan, H. Almohammadi, J. Probst and R. Mezzenga, *Adv. Mater.*, 2021, **33**, 2106155.

151 J. Pérez-Juste, I. Pastoriza-Santos, L. M. Liz-Marzán and P. Mulvaney, *Coord. Chem. Rev.*, 2005, **249**, 1870–1901.

152 J. Gao, C. M. Bender and C. J. Murphy, *Langmuir*, 2003, **19**, 9065–9070.

153 M. J. Han, M. McBride, B. Risteen, G. Zhang, B. V. Khau, E. Reichmanis and D. K. Yoon, *Chem. Mater.*, 2020, **32**, 688–696.

154 M. J. Han, H. S. Yun, Y. Cho, M. Kim, C. Yang, V. V. Tsukruk and D. K. Yoon, *ACS Nano*, 2021, **15**, 20353–20363.

155 M. Chopra, L. Li, H. Hu, M. A. Burns and R. G. Larson, *J. Rheol.*, 2003, **47**, 1111–1132.

156 S. S. Abramchuk, A. R. Khokhlov, T. Iwataki, H. Oana and K. Yoshikawa, *Europhys. Lett.*, 2001, **55**, 294–300.

157 C. A. P. Petit and J. D. Carbeck, *Nano Lett.*, 2003, **3**, 1141–1146.

158 J. Guan and L. J. Lee, *Proc. Natl. Acad. Sci. U. S. A.*, 2005, **102**, 18321–18325.

159 H. Yokota, J. Sunwoo, M. Sarikaya, G. Van Den Engh and R. Aebersold, *Anal. Chem.*, 1999, **71**, 4418–4422.

160 B. Li, C. Zhang, B. Jiang, W. Han and Z. Lin, *Angew. Chem., Int. Ed.*, 2015, **54**, 4250–4254.

161 B. Zhang, J. Schmidtke and H. Kitzerow, *Adv. Opt. Mater.*, 2019, **7**, 1801766.

162 S. M. Park, G. Park and D. K. Yoon, *Adv. Mater.*, 2023, 2302135.

163 G. Picard, D. Simon, Y. Kadiri, J. D. LeBreux and F. Ghozayel, *Langmuir*, 2012, **28**, 14799–14807.

164 M. Roman and D. G. Gray, *Langmuir*, 2005, **21**, 5555–5561.

165 G. Chu, R. Vilensky, G. Vasilyev, P. Martin, R. Zhang and E. Zussman, *J. Phys. Chem. Lett.*, 2018, **9**, 1845–1851.

166 H. Maeda, *Langmuir*, 1997, **13**, 4150–4161.

167 Y. Lin, E. Balizan, L. A. Lee, Z. Niu and Q. Wang, *Angew. Chem., Int. Ed.*, 2010, **49**, 868–872.

168 T. Sawada, Y. Murata, H. Marubayashi, S. Nojima, J. Morikawa and T. Serizawa, *Sci. Rep.*, 2018, **8**, 5412.

169 B. Y. Lee, J. Zhang, C. Zueger, W.-J. Chung, S. Y. Yoo, E. Wang, J. Meyer, R. Ramesh and S.-W. Lee, *Nat. Nanotechnol.*, 2012, **7**, 351–356.

170 J. Kim, Y.-S. Choi, G. Park, M. Kim, J. S. Myung, W. J. Choi, S. M. Park and D. K. Yoon, *ACS Nano*, 2023, **17**, 22778–22787.